Journal of Materials Chemistry A

ROYAL SOCIETY OF CHEMISTRY

PAPER

View Article Online
View Journal | View Issue

Cite this: J. Mater. Chem. A, 2025, 13, 7422

Unraveling the CO_2 methanation and capture ability of NiO@metal oxides†

Huldah Suharika Chitturi,‡[a] Yalagandula Lavanya,‡[a] Yaddanapudi Varun,[a] Anurag Ramesh,[a] Sri Himaja Pamu,[a] I. Sreedhar[a] and Satyapaul A. Singh *[ab]

The present study reports the development of different core–shell nanoparticles using Ni/NiO as the core and other active metal oxides such as SiO_2, Co_3O_4, CeO_2 and ZrO_2 as shells for CO_2 methanation. Among all the studied core–shell materials, NiO@SiO_2 and NiO@CeO_2 showed the highest catalytic activity of >62% for CO_2 conversion and >99% selectivity towards CH_4 with a high GHSV of 47 760 h^{-1} at 325 °C. The catalysts were thoroughly tested under lean and realistic feed conditions. XRD revealed the presence of NiO as the dominant core. All these catalysts were further subjected to characterization techniques such as SEM, TEM, XPS, N_2 adsorption–desorption, H_2-TPR, H_2 pulse, and CO_2-TPD-MS to understand their morphology, ionic nature, physical properties, reduction nature, active site dispersion, adsorption of CO_2 and desorption of surface intermediates. Investigation into the formation and consumption of various intermediates *via* DFT studies revealed that the CO_2 methanation reaction proceeds *via* a combination of the CO and formate pathways. These findings correlate with *in situ* FTIR studies, unveiling structure–property relations and methanation mechanisms. At 25 °C, NiO@SiO_2 exhibited a superior CO_2 capture performance of 301.96 mg of CO_2 per g at 50 bar, while NiO@Co_3O_4 adsorbed 90.40 mg of CO_2 per g at 1 bar. Interestingly, H_2 adsorption was nearly uniform across all these materials even at 50 bar and 25 °C. The core–shell materials show CO_2 capture and hydrogenation abilities towards methane formation.

Received 28th October 2024
Accepted 28th January 2025

DOI: 10.1039/d4ta07672a

rsc.li/materials-a

1. Introduction

The global consumption of fossil fuels has steadily increased over time and is projected to continue rising in the coming decades.[1] Industries, power plants, plastic and chemical sectors, and households are among the primary consumers of fossil fuels.[2] This growing demand for energy has led to substantial growth in carbon dioxide emissions.[3] To mitigate CO_2 emissions, various strategies such as absorption,[4,5] stripping,[6,7] adsorption,[8–10] and CO_2 utilization are commercially proven technologies.[11–14] The utilization of CO_2 emission involves CO_2 conversion into value-added products *via* hydrogenation.[15] The Sabatier reaction (or CO_2 methanation reaction) is a hydrogenation reaction that can produce methane at lower temperatures, below 300 °C.[16] It is possible to maintain a sustainable level of carbon energy circulation if hydrogen is produced using the surplus of electrical energy generated by renewable sources.[17] Photosynthesis and photocatalysis are distinct competing approaches to transform carbon dioxide into value-added products.[18–20] Electrochemical CO_2 reduction,[21] biological CO_2 conversion,[22] and thermo-catalytic CO_2 methanation[23] are all latent pathways for reducing greenhouse gas emissions. The conceivable power-to-gas (PtG) processing technologies (thermo-catalytic CO_2 methanation) for use in forthcoming energy systems have been reviewed.[24,25] These technologies permit the conversion of renewable energy into methane through catalytic methanation.[26] The produced methane can be stored or transported *via* the existing natural gas infrastructure, offering flexibility and supporting power grid stabilization with high renewable energy integration. This approach plays a crucial role in enabling long-term economic decarbonization.

The hydrogenation of carbon dioxide to yield renewable methane (CH_4) is thus a promising and sustainable solution.[27] The Sabatier reaction can make use of the abundant CO_2 to produce CH_4, which has high energy density as a fuel and partly fulfils the energy demand.[28,29] Additionally, CH_4 as a fuel leaves a lower carbon footprint than that left by the combustion of other traditional fossil fuel liquids. The Sabatier reaction is shown in eqn (1) below:

$$CO_2 + 4H_2 \rightleftarrows CH_4 + 2H_2O \quad \Delta H^{\circ}_{298K} = -165 \text{ kJ mol}^{-1} \quad (1)$$

[a]Department of Chemical Engineering, Birla Institute of Technology and Science (BITS) Pilani, Hyderabad Campus, Jawahar Nagar, Kapra Mandal, Hyderabad-500 078, India. E-mail: satyapaul@hyderabad.bits-pilani.ac.in; Tel: +91 40 66303 566

[b]Materials Centre for Sustainable Energy & Environment, Birla Institute of Technology and Science (BITS) Pilani, Hyderabad Campus, Jawahar Nagar, Kapra Mandal, Hyderabad-500 078, India

† Electronic supplementary information (ESI) available. See DOI: https://doi.org/10.1039/d4ta07672a

‡ These authors contributed equally to this work.

Ni is an abundantly available transition metal, having a good catalytic property towards methanation reaction. Several studies have focused on the development of Ni-based catalysts for better yields at low temperature by substitution with other groups of materials, like alkaline earth metals,[30–32] lanthanides[33,34] and noble metals.[35] Zeolites and MOF-based materials are also helpful in developing suitable catalysts towards CO_2 methanation by doping a suitable metal oxide.[36–39] A catalyst must possess crucial properties of strong metal support interaction (SMSI), oxygen storage capacity (OSC) and affinity towards hydrogenation. Furthermore, morphologically tuned materials, particularly core–shell nanoparticles, are effective in achieving these properties, enabling catalytic activity at lower temperatures (below 300 °C) to prevent undesirable reverse water–gas shift reaction (RWGS). Core–shell nanoparticles, made from single or multiple metal oxides or nanocomposites, offer numerous active sites through their core or shell.[40] Additionally, the shell coating improves the core's reactivity, thermal stability, and overall dispersion, making them highly stable and efficient catalysts.[41,42]

Core–shell nanoparticles may be produced using a variety of processes, and the Stöber approach is one of the strategies.[43] These materials possess good thermal stability, high dispersion, and contributes to the confinement of active sites inside the catalytic system matrix.[44] A recent study on Ni–Al@Al_2O_3 showed a very high CO_2 conversion of almost 96% at 310 °C.[45] Apart from Ni-based core–shell nanoparticles, the cobalt-based core shell nanoparticles were also synthesized and showed 56% CO_2 conversion at 400 °C.[46] The MOF-based core–shells with Fe as the dopant enhanced the catalytic ability. In these studies, the catalyst showed 73.2% CO_2 conversion at 350 °C due to Fe–Ni alloy formation.[47] Another study showed significant improvement in the catalytic activity of carbide core–shells with ruthenium as the active metal.[48]

In most studies, the relationship between a material's CO_2 capture ability and its catalytic hydrogenation performance remains underexplored. In this work, core–shell nanoparticles were developed using the modified Stöber method, by choosing NiO as the core and four different materials as shells. NiO nanoparticles were synthesized using the precipitation method. The choice of shells is based on the reduction nature of the materials. Two shell materials, Co_3O_4 and CeO_2, were used as an active metal oxide for providing more OSC, and the other two shells are SiO_2 and ZrO_2 to facilitate SMSI. All materials were well characterized by XRD, XPS, electron microscopy, TPR and N_2 adsorption–desorption techniques to assess the crystallinity, chemical shift, morphology, reducibility, and nature of the isotherms. CO_2 methanation studies were conducted under both lean and realistic feed conditions. DFT calculations were used to examine the reaction pathway. CO_2-TPD coupled with mass spectrometry (MS) provided insights into possible intermediates, and correlated with the DFT findings. Finally, *in situ* FTIR studies with reaction gases and pure CO_2 probing were performed to obtain insight into the reaction mechanisms and CO_2 capture ability. High-pressure CO_2 and H_2 capture studies were performed as a proof-of-concept and further showed the applicability of the core–shell materials at the industrial scale under inevitable high-pressure conditions. To the best of our knowledge, very few studies have been reported on both capture and utilization fronts.[49–55] The present study aims to showcase the possible correlation among capture and utilization.

2. Results and discussion

2.1. X-ray diffraction (XRD) studies

Fig. 1 shows the XRD patterns of the core–shell nanoparticles. The presence of NiO was observed in all catalysts. The peaks at 2θ values of 29.1° and 48.1° represent the CeO_2 phase (JCPDS file number: 00-034-0394)[56] with lattice planes of (111) and (220), respectively. The monoclinic ZrO_2 peaks were identified at 2θ values of 31.5°, 36.3°, 51.8°, 61.4° with lattice planes of (111), (2̄01), (1̄22) and (331) (JCPDS file number: 00-037-1484), respectively.[57] The 2θ values at 18.9°, 31.3°, 36.2°, 44.5°, 59.3° and 65.2° with the lattice planes of (111), (220), (311), (400), (511), (440) (JCPDS file number: 00-043-1003), respectively, represent Co_3O_4 in the cubic phase.[58]

A pure phase of metal oxide NiO formation was observed. Any other impurities, like metal oxide in different crystalline phases, nitrates or metal content, were not found in the XRD patterns. It was observed that there is a slight change in the XRD pattern at 44–46° having a Bragg angle difference. This indicates the formation of defects in the crystalline system during the creation of core–shells. When the NiO@Co_3O_4 XRD pattern were compared with that of the Ni–Co alloy, it was observed that there was no JCPDS file available for the Ni–Co alloy.[59]

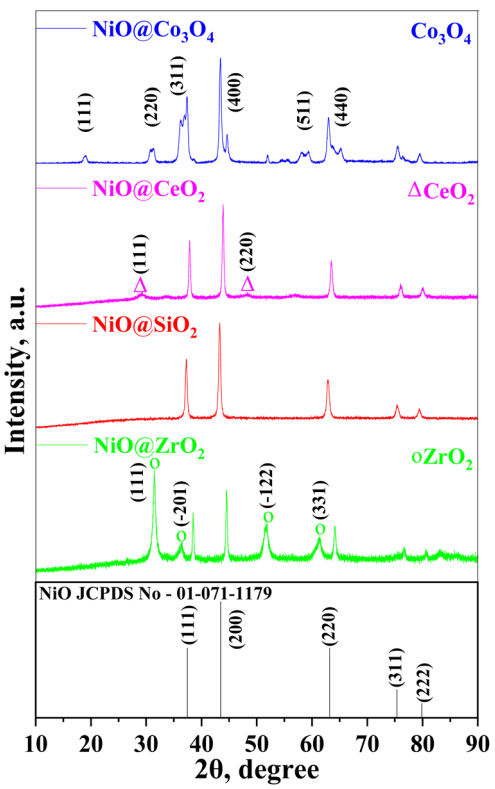

Fig. 1 XRD patterns of the as-prepared core–shell nanoparticles.

In order to know the defect formation, Williamson–Hall studies were performed for all catalysts considering eqn (2).

$$\beta \cos \theta = \frac{K\lambda}{D} + 4\varepsilon \sin \theta \quad (2)$$

where, β is the full-width-half-maxima of the instrumental corrected broadening, θ is the Bragg angle, K is a constant (0.94), λ is the wavelength of incident X-ray (1.5406 Å), D is the crystallite size, and ε is the microstrain, which is obtained from the slope of eqn (2) [$\beta \cos \theta$ *vs.* 4 $\sin \theta$]. The Williamson hall study is used to study the broadening of the peaks in the XRD pattern by calculating the microstrain (ε) and crystallite size (D).[60–64] The Williamson–Hall relation is shown in Fig. S1,† wherein there is a linear fit with a coefficient of determination value of R^2 as 0.969, 0.910, 0.970, and 0.953 for NiO@SiO_2, NiO@CeO_2, NiO@Co_3O_4, and NiO@ZrO_2, respectively. The microstrains of all catalysts are listed in Table S2.†

2.2. Surface area and pore volume analysis

Fig. S2(a, b and d)† shows the type-III isotherms due to the weak interactions, facilitating multi-layer adsorption without the formation of a monolayer. Conversely, Fig. S2(c)† follows a distinctive type IV isotherm, which exhibits the formation of a monolayer at lower pressure regions, succeeded by the formation of multilayers. In this case, it is more likely that the Zr atoms might have occupied the NiO mesopores, which resulted in the decrease in the average pore volume.[65] This observation suggests that the material primarily possesses mesopores with a cylindrical morphology and uniform cross-sectional area. The presence of an H2 type hysteresis loop in the NiO@ZrO_2 system indicates the existence of mesopores characterized by spherical geometry, open terminations, and multiple narrowing's or constrictions. The physical properties of all materials are shown in Table 1.

2.3. Scanning electron microscopy images (SEM)

Fig. 2 depicts micrographs displaying the core–shell nanoparticles. Among the catalysts investigated, NiO@SiO_2 exhibited the most favorable morphology, resulting in the formation of spherical silica particles surrounding the NiO nanoparticles. In all the catalysts, the coverage of the shells was good, except with ZrO_2. The other catalysts, except for NiO@ZrO_2, displayed enhanced morphology attributed to the absence of bulk aggregation. These images effectively demonstrate the intricate nature of the spherical core–shell nanoparticles. In Fig. S3,† EDX analysis confirmed the presence of oxygen in the synthesized catalysts, verifying that the sole type of material generated was metal oxide.

2.4. High-resolution transmission electron microscopy images (HRTEM)

Fig. 3 shows the TEM, HRTEM and SAED pattern analysis of the NiO@metal oxide nanoparticles. The shape of the NiO@SiO_2 nanocomposite is consistent with the formation of core–shell nanoparticles, and the particle size distribution is unique in the form of spheres. The agglomeration is only noticeable where other shell doping is performed in conjunction with surface modification. However, it is still possible to see the essential core–shell structures. This suggests that there is a possibility of a precursor impact being present. Co_3O_4 was discovered at plane (311), and ZrO_2 was discovered at planes (111) and (220), respectively, as shown in Fig. 3(e), (f), (h) and (i), respectively. The NiO planes of (200), (220), and (311) were detected in Fig. 3(e) and (f). The interplanar spacing values obtained from the micrographs show the presence of all shell materials except SiO_2, due to its amorphous nature. The interplanar spacing values of the NiO core found from Fig. 3(b), (e), (h) and (k) were 2.43 Å, 2.39 Å, 2.42 Å and 1.45 Å, respectively, at planes of NiO (111) and NiO (220). For the shell materials from Fig. 3(b), (e), (h) and (k), the *d*-spacing values for CeO_2 (111) is 3.24 Å, ZrO_2 (200) is 2.58 Å, Co_3O_4 (422) is 2.62 Å. SiO_2 is not detected in any plane. However, its presence is visible around NiO. A TEM EDS mapping was performed to identify the presence of Ni, Co, Ce, Zr, and Si, and is shown in Fig. S4.†

2.5. H_2-temperature programming reduction studies

The investigations were conducted using temperature programming, and the results are shown in Fig. 4. At 348 °C, NiO@SiO_2 was significantly reduced, revealing the NiO reduction peak. A shoulder between 300 and 400 °C is likely due to SMSI effects between NiO and SiO_2. This interaction could lead to encapsulation effects, where the NiO interacts with SiO_2 in a manner that alters the reduction profile of NiO.[66] The H_2-TPR study on SiO_2 alone is presented in Fig. S5,† and proves that the shoulder does not correspond to SiO_2 reduction. A similar interaction was observed with the cobalt oxide encapsulation.

Table 1 Physical and structural properties as well as elemental composition and active site analysis

Catalyst	Surface area[a], $m^2\ g^{-1}$	Total pore volume[b], $cm^3\ g^{-1}$	Mean pore diameter[b], nm	Crystallite size[c], nm	Theoretical[d], atom%	%Ni dispersion[d,e]	Ni surface area[e], $m^2\ g^{-1}$	Number of active sites[f], μmol g^{-1}
NiO@Co_3O_4	15	0.23	16	60	20.20	0.19	0.04	661.29
NiO@CeO_2	28	0.14	21	29	21.87	0.42	0.21	1579.8
NiO@ZrO_2	21	0.12	8.0	30	13.98	0.52	0.25	1249.4
NiO@SiO_2	58	0.18	35	59	14.00	0.69	0.34	1651.3

[a] Calculated using BET. [b] Calculated using BJH. [c] Estimated using Debye–Scherrer equation. [d] Determined using ICP-OES. [e] Estimated from the H_2 pulse titration method. [f] Calculated based on H_2 uptake.

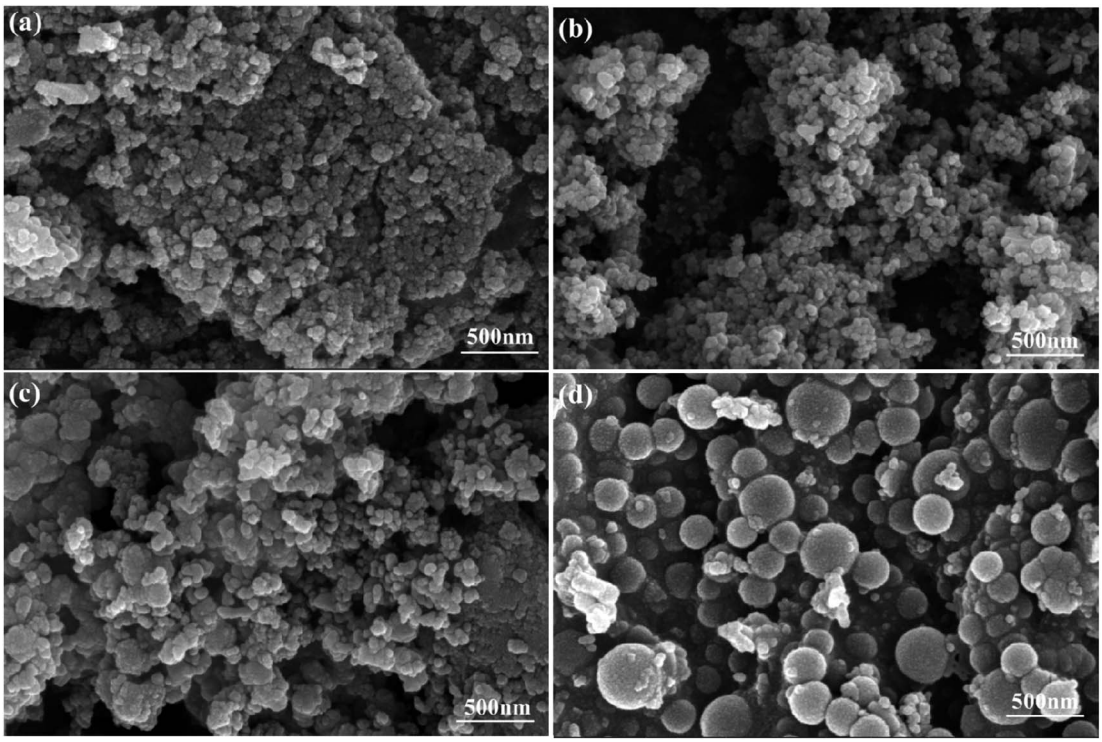

Fig. 2 SEM images of (a) NiO@CeO_2, (b) NiO@Co_3O_4, (c) NiO@ZrO_2 and (d) NiO@SiO_2.

The NiO reduction was seen at 332 °C, indicating that NiO and Co_3O_4 were reduced at the same temperature and formed a bulk nanocomposite, leading to the greater NiO and Co_3O_4 interaction. All catalysts showed reduction peaks to NiO between 250 and 500 °C. Multiple reduction peaks at various temperatures in the NiO@CeO_2 catalyst demonstrate the presence of various oxidation states. The NiO@ZrO_2 system showed a second peak at around 445 °C, indicating a nanocomposite emergence. This peak likely corresponds to the reduction of NiO facilitated by the ZrO_2 support, which can promote reducibility through oxygen mobility and the creation of active sites at the interface. The emergence of nanocomposites during this process further supports the idea that the peak is linked to structural and electronic changes, rather than the direct reduction of the ZrO_2 support. For NiO@ZrO_2, the attribution of the reduction peak to nanocomposite formation is reasonable, and aligns with the known properties of ZrO_2.

NiO@ZrO_2 and NiO@CeO_2 show reduction peaks at 362 °C and 305 °C, respectively. This suggests that the interactions between NiO and ZrO_2 are low by forming Zr^{4+} ions and those with CeO_2 are strong by forming Ce^{4+} ions, indicating the low area in the peak. One of the reasons that ZrO_2 interacts less effectively with other nanoparticles is its lack of a porous structure, which is commonly found in other core–shell nanoparticles. This might cause very low catalytic activity when ZrO_2 is used as the shell. Consumption of H_2 for core–shell nanoparticles was calculated and presented in Table 2.

H_2-TPR analysis also assesses the Oxygen Storage Capacity (OSC) of materials, which is an ability of materials to store and release oxygen. The OSC of the material depends on the reducibility of the catalyst. As the reaction progresses, lattice vacancies are created due to the consumption of lattice oxygen atoms. These vacancies subsequently capture oxygen-centric molecules from the reactants, thereby enhancing the OSC of catalyst and contributing to the reaction pathway. Notably, both CeO_2 and Co_3O_4 materials exhibit a robust oxygen storage capacity (shown in Table 2).

2.6. CO_2-temperature programming desorption studies

The basicity of the synthesized core–shell nanoparticles was investigated using CO_2-TPD, and is shown in Fig. 5(a). These profiles demonstrated the presence of weak, medium, and strong basic sites. The maxima temperatures for weak basic sites were observed in the temperature range of 84 °C to 189 °C for all catalysts. The reduction of the catalysts has enhanced the surface basicity of the catalysts. Except for NiO@Co_3O_4, all catalysts showed CO_2 desorption from room temperature to 800 °C, indicating the distribution of basic sites across all temperatures. Both the weak and strong basic sites are found to be more prominent than the medium basic sites. NiO@SiO_2 has a large number of weak (283.5 μmol g^{-1}) and medium basic sites (45.08 μmol g^{-1}) among all catalysts, hinting its ability for CO_2 methanation activity. NiO@CeO_2 also offered a good number of weak basic sites (229.0 μmol g^{-1}), which contributes to 84.7% of the total basic sites. However, a total of only 4.85% of the medium and a notable 10.4% of the strong basic nature was witnessed.

Both NiO@Co_3O_4 and NiO@ZrO_2 had very low weak basic sites of 26.59 and 38.62 μmol g^{-1}, respectively. The medium

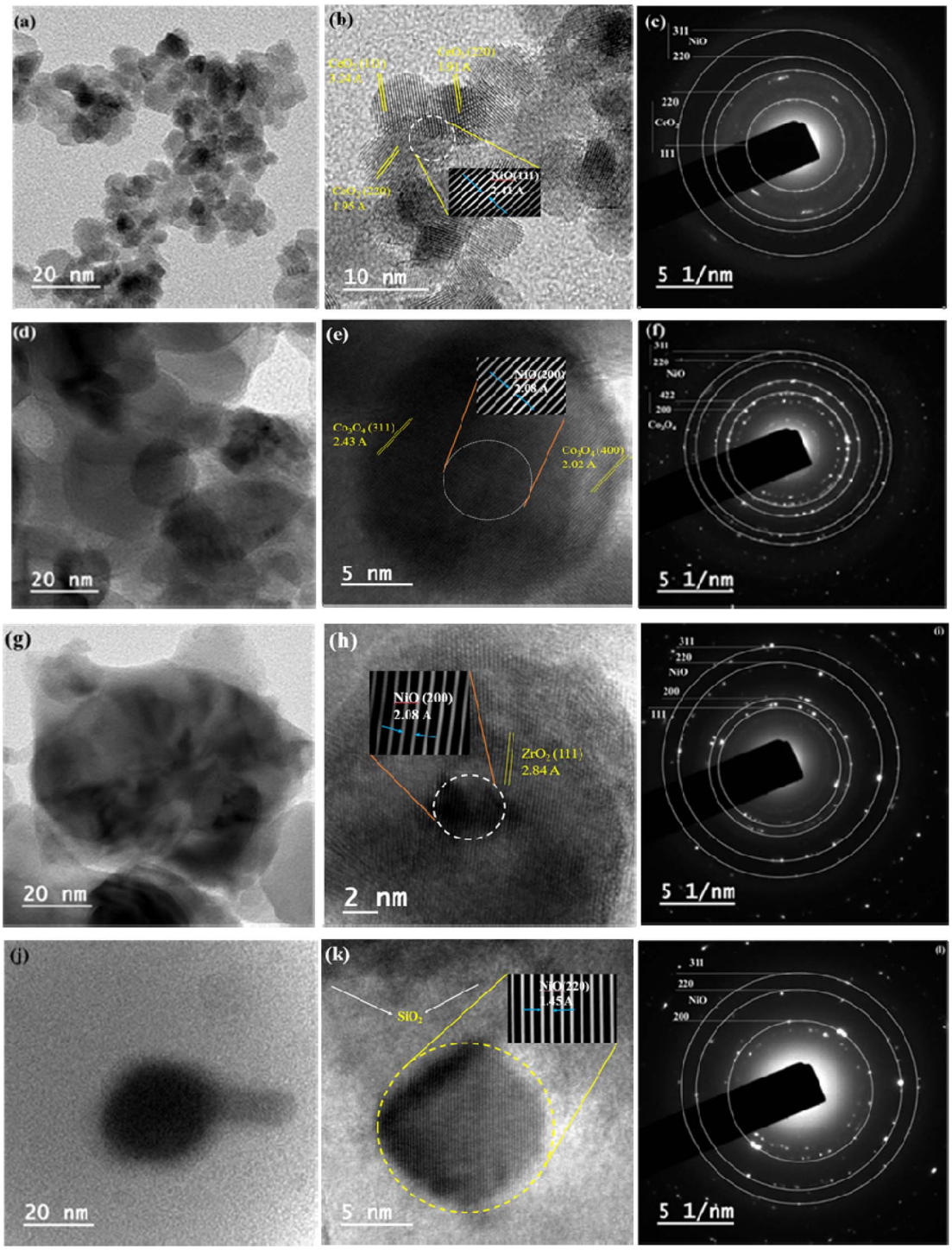

Fig. 3 TEM, HRTEM and SAED patterns of (a–c) NiO@CeO_2, (d–f) NiO@Co_3O_4, (g–i) NiO@ ZrO_2 and (j–l) NiO@SiO_2 (insets of (b), (e), (h) and (k) show fast Fourier transform (FFT) images).

basicity was not observed among these two catalysts. This hints that both catalysts may not be highly active for CO_2 methanation. A peculiar outcome has been observed for the NiO@ZrO_2 catalyst. It showed the presence of a large number of strong basic sites at the temperature range of 650 °C to 860 °C. A significant value of 638.9 μmol g^{-1}, contributing to 94.3% of the total basicity, was measured as the strong basic sites. This indicates that NiO@ZrO_2 may offer good catalytic activity for high-temperature reactions, such as dry reforming of methane rather than CO_2 methanation.

A mass spectrometer connected to the CO_2-TPD instrument enables qualitative analysis of CO_2, CO, and other gases during temperature ramping, as shown in Fig. 5(b–f). This technique identifies functional groups based on their thermal

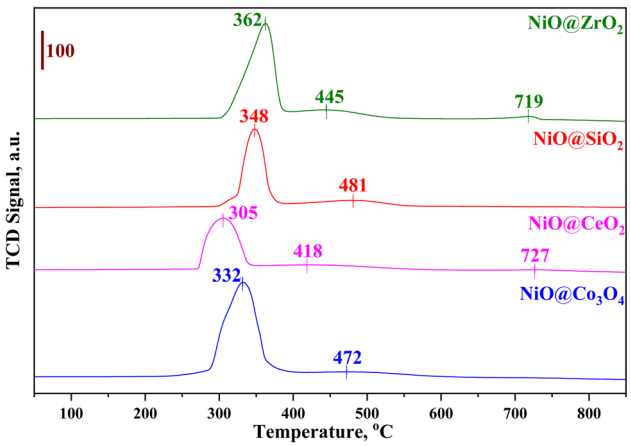

Fig. 4 H_2-TPR studies on core–shell nanoparticles NiO@S, where S = CeO_2, SiO_2, Co_3O_4 and ZrO_2.

decomposition with temperature being a crucial parameter. The desorbed CO_2 gas is detected by the mass spectrometer in the form of CO_2 ($m/z = 44$), CO ($m/z = 28$), and CH_4 ($m/z = 16$) (as shown in Fig. 5(f), (e) and (c)). The presence of hydrogen is possible due to the H_2 reduction step in the catalyst pretreatment, which is further confirmed from the detection of both atomic and molecular hydrogen ($m/z = 1$ and 2, as shown in Fig. 5(b)). Furthermore, as the reduction step also weakens the metal–oxygen bond and simultaneously dissociates CO_2 by utilizing created oxygen vacancies, the atomic and molecular oxygen ($m/z = 16$ and 32) will thus be released during the TPD study (as shown in Fig. 5(c)).[67] Although both CH_4 and atomic oxygen are identified at the same $m/z = 16$, the detected $m/z = 32$ for molecular oxygen and the formation of water (with $m/z = 18$ shown in Fig. 5(d)) proves the release of oxygen. These crucial details from CO_2-TPD-MS experimentally support the mechanism developed by DFT studies.

2.7. H_2 pulse chemisorption

Utilizing the H_2 pulse chemisorption technique, the active Ni dispersion and its surface area in all four catalysts were estimated. The metal dispersion was calculated from eqn (3).

$$\%\ \text{dispersion} = \frac{N \times M_{Ni}}{N_{Ni} \times SF} \times 100 \quad (3)$$

where, N is the number of active sites, M_{Ni} is the molecular weight of Ni, N_{Ni} is the % metal loading (obtained from ICP-OES), and SF is the stoichiometric factor. Table 1 summarizes the results, highlighting a substantial metal dispersion of 0.69% and 0.52% for NiO@SiO_2 and NiO@ZrO_2, whereas NiO@CeO_2, NiO@Co_3O_4 showed the dispersion values as 0.42%, 0.19%, respectively. Notably, the active metal surface areas of NiO@SiO_2, NiO@CeO_2, NiO@Co_3O_4, and NiO@ZrO_2 were estimated as 0.34, 0.21, 0.04, and 0.25 $m^2\ g^{-1}$ through H_2 chemisorption, respectively. This analysis supports the assertion that NiO@SiO_2 boasts a higher metal dispersion of the active metal, coupled with increased surface area, potentially contributing to enhanced catalytic activity compared to the other catalysts. Even though NiO@ZrO_2 has demonstrated a high metal dispersion, the activity was very low when compared with the other catalysts due to its insignificant weak and medium basic sites. The H_2 pulse graphs of all catalysts are presented in Fig. S6.† The H_2 pulse chemisorption was also performed without a reduction step. A clear improvement in the active metal surface area was observed upon the reduction step, and it is reported in Table S3.†

3. Catalytic activity studies

The catalytic activity of each core–shell catalyst is shown in Fig. 6(a and b) for the low feed concentrations and Fig. 6(c) for the high feed concentrations. The temperature range of 150 °C to 400 °C was used to investigate the catalytic activity. The NiO catalyst without reduction has shown 38% CO_2 conversion at 375 °C, and 51% of CO_2 conversion was attained by the NiO catalyst with reduction at 400 °C. In terms of the methane selectivity, >90% was achieved by both the reduced and the non-reduced NiO catalyst, and the graphs are presented in Fig. S7.† Apart from the ZrO_2-based shell material, the catalytic activity of the synthesized core–shell nanoparticles was found to be excellent. At a temperature of 250 °C, all materials exhibited decent CO_2 conversion. The initial temperature also has a significant impact on the rate of CO_2 conversion. The light-off curve began at 225 °C for NiO@ZrO_2 and it is almost inert, which can be proved from the low pore volume of 0.12 $cm^3\ g^{-1}$, and low weak and medium basicity, as shown in Tables 1, 2, and in Fig. 5. Thus, it is possible that zirconia covered most of the active sites accessible in the catalyst system, which might be the reason for such poor catalytic activity. The other three shells exhibited good catalytic activity toward methanation. However, NiO@SiO_2 has better performance compared to the other materials. The selectivity toward methane is excellent (100% of methane selectivity) up to 325 °C for all catalysts. In Fig. 6(c), it was observed that the light-off curves started after 200 °C for the

Table 2 H_2 consumption and surface basicity of the catalysts

		Surface basicity based on CO_2 desorption, μmol g^{-1}			
Catalyst	Total H_2 consumption, μmol g^{-1}	Weak	Medium	High	Total
NiO@Co_3O_4	17 632	26.59 (100%)	—	—	26.59
NiO@SiO_2	10 003	283.5 (59.3%)	45.08 (9.43%)	149.5 (31.3%)	478.1
NiO@ZrO_2	15 099	38.62 (5.70%)	—	638.9 (94.3%)	677.5
NiO@CeO_2	10 949	229.0 (84.7%)	13.11 (4.85%)	28.18 (10.4%)	270.3

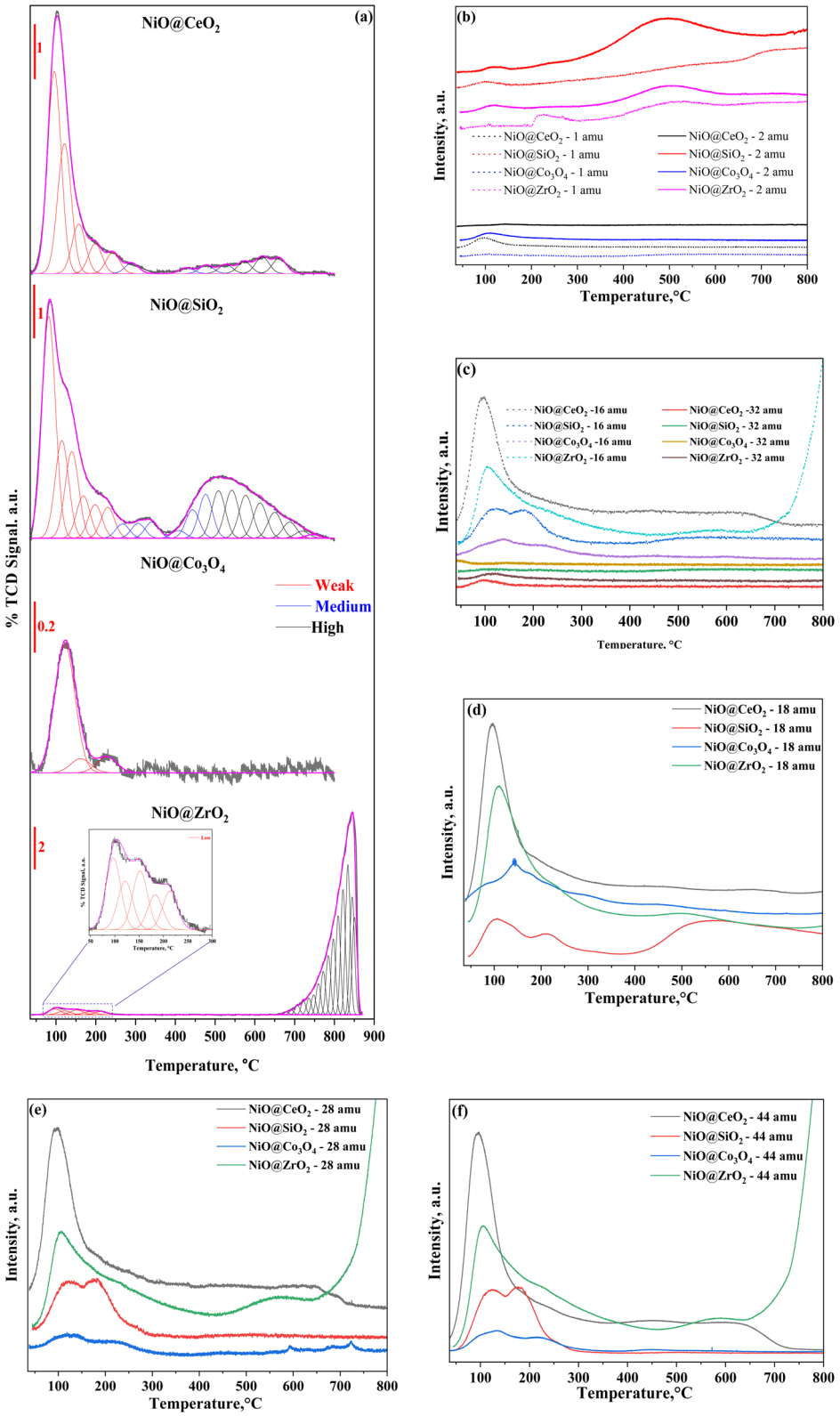

Fig. 5 (a) CO_2-TPD, CO_2-TPD MS profiles of core–shell nanoparticles at an m/z of (b) 1 and 2, (c) 16 and 32, (d) 18, (e) 28 and (f) 44.

best catalysts due to high concentrations in the feed. At the temperature of 325 °C, NiO@CeO_2 and NiO@SiO_2 showed 62% and 67% of CO_2 conversion, respectively. After that, the NiO@CeO_2 conversion was increased to 72% at 400 °C. For NiO@SiO_2, there was a decline in conversion. However, in terms of %CH_4 selectivity, NiO@SiO_2 had 100% selectivity. For

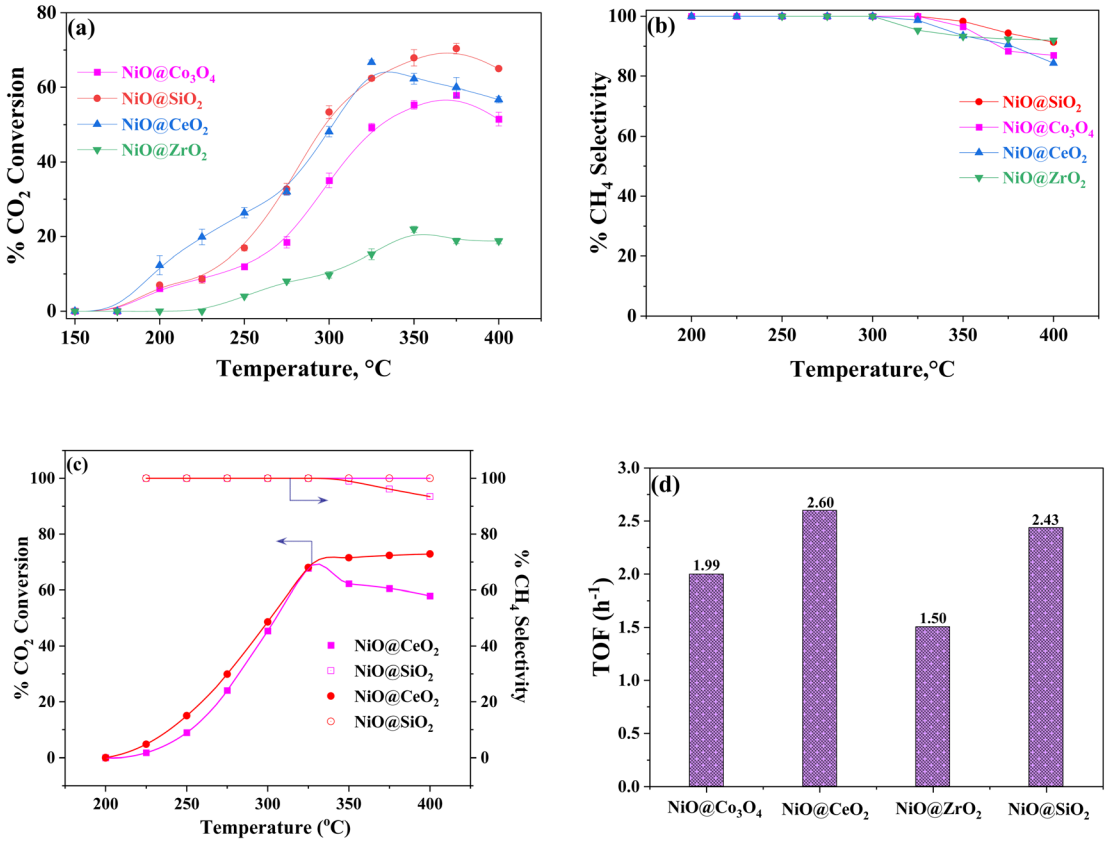

Fig. 6 Catalytic activity studies plot of the (a) %CO_2 conversion and (b) %CH_4 selectivity for the core–shell catalysts NiO@S (where S = CeO_2, SiO_2, Co_3O_4 and ZrO_2; $CO_2 : H_2 : N_2$ = 2 : 8 : 90 vol%; catalyst loading = 200 mg; and GHSV = 47 760 h^{-1}), (c) %CO_2 conversion and %CH_4 selectivity for NiO@SiO_2 and NiO@CeO_2 with flowrates of ($CO_2 : H_2 : N_2$ = 10 : 40 : 50 vol%, catalyst loading = 200 mg, GHSV = 47 760 h^{-1}), and (d) TOF of all catalysts at 350 °C.

NiO@CeO_2, there was a decrease in the selectivity, as there was the formation of CO as a byproduct. The oxide–NiO interaction could enhance the catalyst's ability to adsorb and activate CO_2, while influencing the hydrogenation steps to improve the overall efficiency and selectivity of the methanation reaction.[68]

Turnover frequencies (TOF) of the catalysts were evaluated to normalize the catalytic activity of all catalysts containing different active site compositions, and is expressed as follows:

$$\mathrm{TOF} = \frac{F_{CO_2} \times X_{CO_2}}{W_{cat} \times N_{Ni}} \quad (4)$$

where, W_{cat} is the mass of the catalyst in g, F_{CO_2} is the molar flowrate of CO_2 and N_{Ni} is the molar amount of Ni atoms present per g of catalyst. From Fig. 6(d), NiO@CeO_2 and NiO@SiO_2 have shown the highest turnover frequency compared to the other catalysts. These two catalysts are identified as the highly active catalysts among all.

In Fig. 6(b), the selectivity of methane steadily decreased with the reaction temperature, showing a weaker inclination towards the methane selectivity after 325 °C for all core–shell catalysts. This is because of CO formation as a byproduct due to the reverse water gas shift reaction at higher temperatures.[69] The NiO@SiO_2 catalyst exhibited excellent methane selectivity and the strongest catalytic activity, even at higher temperatures. Furthermore, SiO_2 has a unique capacity to adsorb CO_2 and provide H_2 with time to react with it. This ability is beneficial to induce the dual role of CO_2 capture and utilization.

The findings of the XRD analysis indicated that all materials were formed in the pure form of metal oxide, and the results of the EDX examination and elemental mapping supported these findings. The presence of metal oxides in its purest form confers several benefits, one of which is the enhancement of the efficiency for producing strong interactions between the metal and the active material.[70–74] The crystallite size of the NiO@SiO_2 material was 59 nm, and it has a high surface area that is observable among all materials. This suggests that SiO_2 shells can effectively distribute over NiO. Furthermore, even better exposure of active sites is possible due to its porous nature.[75] This will promote the best methane selectivity and conversion of CO_2 at lower temperatures. Other than SiO_2, both CeO_2 and Co_3O_4 materials also show better catalytic activity. This may be due to the high OSC, which allows the catalyst to offer more active vacant oxygen sites for the reaction. The presence of Ni^{2+} and Ni^{3+} ions in NiO, as shown in Fig. S7(a),† plays a critical role in activating the reactants, making the catalyst highly active even at low temperatures. The pure NiO was also evaluated for CO_2 methanation, and it was found to be fairly active in its pure phase. However, reduced Ni is found to be more active. In core–

shell catalyst systems, the possible reoxidation of reduced NiO cannot be ignored due to the dissociation of the CO_2 molecule and OSC of the supporting metal oxides. The constructive interaction with other metal oxides offers the CO_2 methanation ability. In general, the ratio of lattice oxygen to vacant oxygen is another factor that contributes to the activation of a catalyst. In conclusion, the oxygen vacancies result in (i) considerable hydrogen coverage augmentation on the support[71,76] and (ii) acts as adsorption sites for CO_2 and its further activation, resulting in the better catalytic activity of the core–shell catalysts.[58,72,77] Table 3 presents a comparative analysis of various catalysts used for CO_2 methanation based on the literature.

3.1. Apparent activation energy studies

Apparent activation energy studies were performed on the catalysts by changing the loading of the catalyst from 0 mg to 200 mg in the interval of 50 mg. The activation energies were calculated by assuming the packed reactor as a differential flow reactor with negligible resistance towards mass transfer and heat transfer. The experimental conversions were plotted as a function of catalytic loading to validate the operation of the kinetic regime. The experimental findings were consistent with the Weisz–Prater correlation for the chosen operating conditions, and therefore validates the differential flow reactor assumption.[89] Considering this, the reaction rates were determined by eqn (5),

$$-r_{CO_2} = \frac{X_{CO_2}}{\left(\frac{W_{cat}}{F_{CO_2}}\right)} \quad (5)$$

$-r_{CO_2}$ = observed reaction rate, μmol g^{-1} s^{-1}, X_{CO_2} = fractional conversion of CO_2, W_{cat} = catalyst loading, g, F_{CO_2} = molar flowrate, μmol s^{-1}.

From Fig. S8(a), (c) and (e),† the fractional CO_2 conversion varies linearly with the catalyst loading in the reactor. The reaction rates for each catalyst were determined from the slope of X_{CO_2} *vs.* $\left(\frac{W_{cat}}{F_{CO_2}}\right)$, which was carried out at several temperatures. From the Arrhenius plots (Fig. S8(b), (d) and (f)†), the apparent activation energies of each catalyst were determined for CO_2 methanation. The catalysts apparent activation energies are NiO@S (S = Co_3O_4, CeO_2, and SiO_2) are 89.0 ± 2, 104 ± 1 and 82.0 ± 2 kJ mol^{-1}, respectively. NiO@ZrO_2 was not considered due to its poor catalytic activity.

3.2. Stability studies

The influence of the time-on-stream condition over the core–shell nanoparticles is shown in Fig. 7. Based on the light-off curve plot (shown in Fig. 6), the temperature effect was investigated for the best catalysts, NiO@SiO_2 and NiO@CeO_2. The catalysts were subjected to 300 °C, at which the side reactions are prominent. Compared to NiO@CeO_2, the conversion and selectivity of NiO@SiO_2 are good, maintaining the same conversions for up to 20 h. A decreasing trend was observed in conversion and selectivity from 35% to 28% and 100% to 87%, respectively. The CO_2 conversion of the NiO@SiO_2 catalyst decreased at first from 51% to 41% and methane selectivity from 98% to 91%, which is minimal. The NiO@SiO_2 core–shell nanoparticles are more stable than NiO@CeO_2 core–shell nanoparticles. Fig. 7(c) presents the %CO_2 conversion for cyclic study, in which each cycle was carried out for 10 h with the gap of 6 h for the NiO@SiO_2 and NiO@CeO_2 catalysts. This makes an effective 50 h time-of-stream to compare with the stability study using lean feed concentrations. The NiO@SiO_2 catalyst has shown fair stability with a maximum drop of 8% in CO_2 conversion for each cycle. Conversely, the drop in conversion is more than 10% using NiO@CeO_2, making it less stable than NiO@SiO_2. However, methane selectivities were found to be >98% for both catalysts throughout the cyclic stability study. Most often, the CO presence was not observed at different times of the cyclic stability study. The aggregation of the active species and the deposition of carbon often leads to the deactivation of this kind of catalyst when it is subjected to high temperatures.[90] This unfavorable occurrence is found to be less prominent when conducted at lower reaction temperatures and is a result of the porous structure, allowing for additional interactions between the core and shell. After the stability studies, the catalysts were subjected to XPS analysis, where it was found that there is no change in the binding energies positions. However, a significant transition from Ni^{2+} to Ni^{3+} was observed with a maximum change in the binding energy of 0.1 eV.

3.3. X-ray photoelectron spectroscopy studies

The core level spectra of the core–shell nanoparticles are shown in Fig. 8. Examination with XPS makes it feasible to establish whether the catalyst has an ionic structure. From the XPS findings, it is possible to accurately forecast information on the electronic structure and composition of Ni, Co and Zr. In this analysis, the fresh and reduced samples are denoted as NiO@S-F and NiO@S-R, where S = CeO_2, SiO_2, Co_3O_4 and ZrO_2. Fig. 8(a and b) depicts the presence of the $2p_{3/2}$ and $2p_{1/2}$ split orbitals of Ni, corresponding to NiO@Co_3O_4-F and NiO@ZrO_2-F, respectively. The Ni^{3+} ions are observed *via* the $2p_{3/2}$ orbital at 856.3 eV and the $2p_{1/2}$ orbital at 871.5 eV. Conversely, the Ni^{2+} ions are observed at 854.0 eV and 871.5 eV at $2p_{3/2}$ and $2p_{1/2}$ orbitals respectively, and the satellite shakeup peaks were detected at 861.3 eV and 879.6 eV, respectively.[91–96] Meanwhile, the NiO@Co_3O_4-R and NiO@ZrO_2-R catalysts resulted in no change in the binding energies after reduction. The O 1s spectra, shown in Fig. S9,† reveal the presence of Ni^{2+} and Ni^{3+} ions at the $2p_{3/2}$ orbital. These ions share the same energy level as all catalysts and the lattice oxygen is at 529.7 eV, vacant oxygen at 531.5 eV and hydroxyl group at 532.6 eV for the NiO@Co_3O_4 fresh catalyst and for the reduction catalyst. It was observed that the peak intensity was increased when compared to the fresh catalyst, and a satellite peak was identified at 534.3 eV for NiO@Co_3O_4-R.[97] Two characteristic peaks were observed at 182.3 eV and 184.5 eV, indicating the $3d_{5/2}$ and $3d_{3/2}$ orbitals, respectively. At 186.1 eV, a satellite peak was observed.[98,99] The O 1s spectra for NiO@ZrO_2 is presented in Fig. S9(b),† in which the lattice oxygen was at 529.8 eV, vacant oxygen was at 531.7 eV and the hydroxyl peaks were at 532.6 eV for the fresh catalyst. For the

Table 3 Literature comparison for CO_2 methanation studies[a]

Catalyst	Method of synthesis	Ni content (wt%)	Temperature, °C	GHSV, h^{-1}/composition [$CO_2 : H_2 : N_2$], vol% or ratio/flowrate, mL min^{-1}	$\%CO_2$ conversion	$\%CH_4$ selectivity	Apparent activation energy, kJ mol^{-1}	Remarks on stability	Ref.
Ni/ZrO_2	Impregnation	10.4[a]	350	30 000, NA, NA	~85	100	71.7	Stability study was not performed	78
$Ni–CeO_2$	Wet impregnation	15.0[c]	360	13 333, 1 : 4 ratio [$CO_2 : H_2$], 200	84	99	—	Stability study of 8 h was conducted, in which the catalyst was stable with CO_2 conversion of 76–77% and selectivity of 99%	79
$Ni–CeO_2$	Wet impregnation	10.2[a]	300	6000, 19 : 76 : 5, NA	84	100	—	100 h of stability test was presented, and there was a decrease in conversion of 1% (84.1–83.6%), while the selectivity was 100%	80
$La_{2-x}Ce_xNiO_4$	Sol–gel	11.2[a]	350	10 000, 1 : 4 ratio [$CO_2 : H_2$], NA	79	99	—	The conversion and selectivity of 78.9% and 100% was obtained. The catalyst is stable throughout the stability study of 100 h	81
$Ni_xFe@C$	Pyrolysis	53.7[a]	350	NA, 23.5 : 70.5 : 6.0, NA	72	99	—	The catalyst has shown a stability at 53.3% of CO_2 conversion, and a selectivity of 100% for the whole 50 h study	47
$80Ni–Zn/SiO_2$	Ammonia evaporation	20.4[a]	300	9000, 1 : 4 ratio [$CO_2 : H_2$], 30	80	100	87.9	73.2% of CO_2 conversion was achieved, and it was stable for 40 h of the stability study	82
$4\%\ Ru/Al_2O_3$	Wet incipient impregnation	3.80[b]	400	10 000, 1 : 5 : 1.5 [$CO_2 : H_2 : He$], NA	80	—	84.0	Time-on-stream study of 24 h was executed, in which there was a decrease in conversion from 81.5% to 78%, while the selectivity was stable at 98%	83
$Ni/Al@Al_2O_3$	Deposition–precipitation	10.0[a]	350	NA, 1 : 50 : 49, 100	96	—	74.0	There was a decrease in conversion for 10 h, but after that, there was a stable conversion of 95% for the 50 h study	45
15%Ni@MGC	Wetness impregnation method	15.0[c]	400	36 000, 1 : 4 : 1 ratio, 60	50	96	75.3	The catalyst showed a stable value of 50% conversion and 96% selectivity for 30 h	84
Ni/ZrO_2	Wetness impregnation method	8.68[a]	350	60 000, 8 : 32 : 10, NA	79	76	93.6	The conversion of 72% was stable for 10 h	85
Ni@C	Pyrolysis	79.0[d]	325	33 000, 1.5 : 6 ratio, 55	100	99	85.3	The stability test was carried out at 250 °C for 24 h and a stable value of 25.3% of CO_2 conversion was obtained	86
$Ni/CeO_2/Al_2O_3$	Impregnation method	15.0[c]	350	21 500, 1 : 4 ratio [$CO_2 : H_2$], NA	68	99	74.0	The stability study of 90 h was performed, and there was approximately 68% of CO_2	87

Table 3 (*Contd.*)

Catalyst	Method of synthesis	Ni content (wt%)	Temperature, °C	GHSV, h^{-1}/composition [$CO_2 : H_2 : N_2$], vol% or ratio/flowrate, mL min^{-1}	$\%CO_2$ conversion	$\%CH_4$ selectivity	Apparent activation energy, kJ mol^{-1}	Remarks on stability	Ref.
								conversion and the CH_4 selectivity was >99%	
$Ni/ZrO_2–Al_2O_3$	Co-precipitation method	18.2[a]	280	48 000, NA	84	99	69.2	The stability tests were not explored	88
$NiO@CeO_2$	Modified Stöber method	32.37[a] (21.87 at%)	325	47 760, 10 : 40 : 50, 100	62	100	104 ± 1	An ~8% drop in CO_2 conversion and 100% selectivity was observed throughout the 50 h stability study	Present study
$NiO@SiO_2$	Modified Stöber method	43.34[a] (14.00 at%)	325	47 760, 10 : 40 : 50, 100	67	100	82.0 ± 2	During the 50 h stability study, ~10% drop in CO_2 conversion and 100% selectivity was observed throughout	Present study
$NiO@Co_3O_4$	Modified Stöber method	39.08[a] (20.20 at%)	375	47 760, 2 : 8 : 90, 100	55	93	89.0 ± 2	—	Present study

[a] Obtained from (a) ICP-OES/MS/AES, (b) H_2-TPR, (c) synthesis method, and (d) EDX.

reduced catalyst, there was a decrease in peak intensity for lattice oxygen with an increase in the vacant oxygen, as there was an oxygen vacancy due to the reduction step. In the $NiO@Co_3O_4$ sample (for both F and R), distinct peaks are observed at 779.8 eV and 794.8 eV, corresponding to the $2p_{3/2}$ and $2p_{1/2}$ orbitals of Co^{3+} ions, respectively. Additionally, Co^{2+} ions are identified by the presence of peaks at 781.7 eV and 796.9 eV, corresponding to the $2p_{3/2}$ and $2p_{1/2}$ orbitals, respectively. The other two satellite peaks are shown in Fig. S10(a).†[77,100,101] The surface of NiO can capture electrons from the conduction band of other materials, giving it the ability to possess ultra-low nanoparticle size. The high electron affinity of NiO captures shell electrons, forming a type-I heterojunction, with the band alignment estimated *via* Tauc plots and Mulliken's theory, as presented in Table S4.† A larger conduction band offset strengthens the core–shell interactions, increasing the surface area and activity in $NiO@SiO_2$ and $NiO@CeO_2$. However, in $NiO@ZrO_2$, the high offset creates an energy barrier that limits electron transfer and reduces the surface area. Similarly, in $NiO@Co_3O_4$, the weaker electron pull also lowers the surface area.[76,102,103]

The characteristic peaks for both Ni^{2+} and Ni^{3+} ions are observed in the $2p_{3/2}$ and $2p_{1/2}$ orbitals. These findings conclusively confirm the formation of NiO.[74,104] With respect to $NiO@CeO_2$, the possibility of finding Ni $2p_{1/2}$ orbitals is unclear due to the overlapping of binding energies in the range of 845 to 870 eV. Fig. S9(c)† presents the oxygen spectra for $NiO@CeO_2$, in which the peak at 530.9 eV represents the lattice oxygen and 532.7 eV represents the vacant oxygen. The peaks at 532.6 eV show the hydroxyl group, and the satellite peak is observed at 534.6 eV for the fresh catalyst. Meanwhile, the reduced catalyst does not show the hydroxyl group, and the other peaks were matched with the fresh catalyst oxygen peaks. The oxygen spectra for $NiO@SiO_2$ are depicted in Fig. S9(d),† in which the peak at 530.4 eV corresponds to lattice oxygen. Meanwhile, the peak at 532.9 eV represents vacant oxygen for both fresh and reduced catalysts, but there was no hydroxyl group peak in the reduced sample. From Fig. S10(c),† the binding energies of 882.0 eV, 889.7 eV, and 897.8 eV were assigned to Ce^{4+} $3d_{5/2}$, while 884.6 eV and 881.3 eV corresponds to the $3d_{5/2}$ orbital of Ce^{3+}. The binding energies of the Ce^{3+} $3d_{3/2}$ orbitals were observed at 889.9 eV and 903.2 eV, and the Ce^{4+} $3d_{3/2}$ orbitals were observed at 900.6 eV, 906.6 eV and 916.4 eV.[105–107]

3.4. Density functional theory (DFT) studies for mechanism investigation

To identify the role of active sites, catalytic activity studies were performed on reduced and non-reduced NiO@S catalysts (where S = SiO_2, CeO_2, Co_3O_4, and ZrO_2), as shown in Fig. 6(a–c). It clearly identifies reduced NiO (probably Ni) as the active site. However, as the reaction further proceeds, the possible re-oxidation of Ni due to atomic oxygen cannot be ignored. This aspect has been highlighted in the CO-mediated pathway, as shown later in the *in situ* FTIR study. Thus, the synergy between both Ni and NiO must be considered to fully understand the reaction pathways.

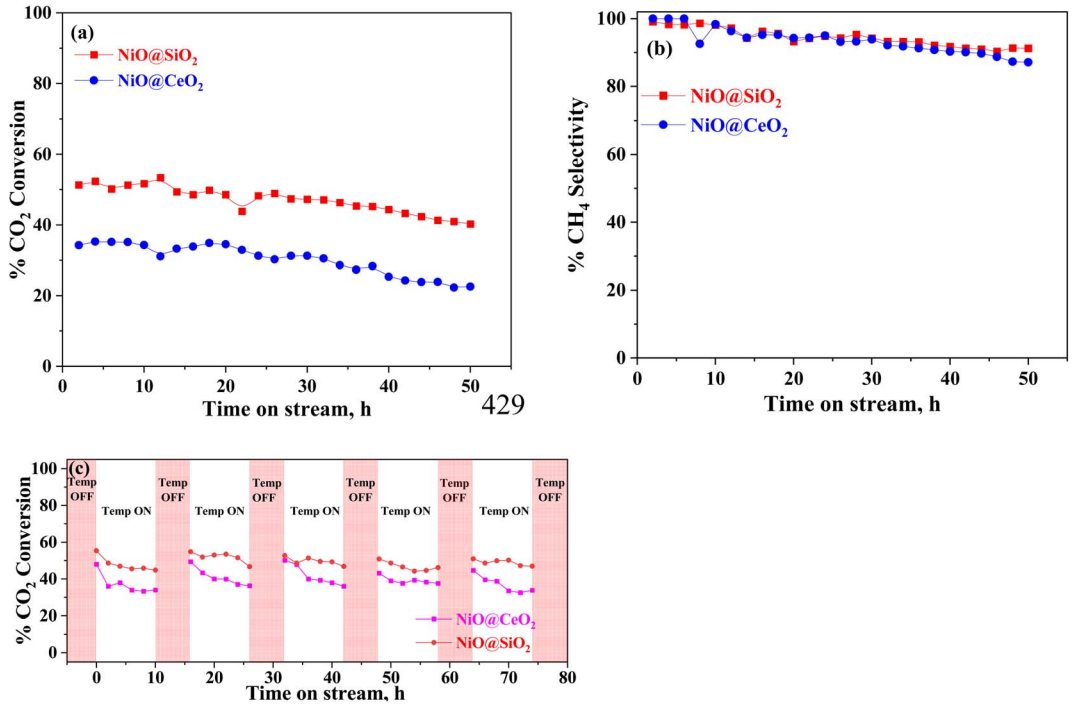

Fig. 7 Time-on-stream studies for (a) %CO_2 conversion, (b) %CH_4 selectivity of the NiO@SiO_2 and NiO@CeO_2 catalysts (CO_2 : H_2 : N_2 = 2 : 8 : 90 vol%, catalyst loading = 200 mg, GHSV = 47 760 h^{-1}, temperature = 300 °C), (c) %CO_2 conversion of NiO@SiO_2 and NiO@CeO_2 catalysts (CO_2 : H_2 : N_2 = 10 : 40 : 50 vol%, catalyst loading = 200 mg, GHSV = 47 760 h^{-1}, temperature = 300 °C).

The role of the Ni active sites has been thoroughly elucidated previously. Ren *et al.* investigated the reaction mechanism of the CO_2 methanation on the Ni (111) surface using DFT calculations. The formation of HCOO* has a relatively low energy barrier, making it a kinetically favorable step. However, the RWGS pathway starts with the conversion of CO_2 to CO, which requires overcoming a higher energy barrier, making it less favorable. The subsequent hydrogenation of CO by intermediates, such as COH*, CHO*, and CH*, to form CH_4 involves a higher activation energy compared to the corresponding steps in the formate pathway. The activation energy of the rate-determining step in the formate pathway is 0.85 eV, compared to 1 eV for the RWGS pathway. This lower energy value associated with the intermediates of the formate pathway indicates its relatively higher stability, making it the preferred pathway for CO_2 methanation on Ni(111) surfaces.[108] Similarly, Jin Huang *et al.* investigated the mechanisms of carbon dioxide methanation in Ni/MgO catalysts with both CO and formate pathways. In the formate pathway, CO_2 is adsorbed on the MgO support, forming carbonate species that are hydrogenated to formate (HCOO*). This formate is then hydrogenated to HCO*, H_2CO*, H_3CO*, and finally CH_4. In the CO pathway, CO_2 is first reduced to CO, which is adsorbed on the Ni surface and hydrogenated by intermediates, such as COH*, CHO*, and CH*, to form methane. The activation energy of the rate-determining step of the formate pathway in Ni/MgO is about 0.78 eV, which is smaller than the corresponding step with Ni alone. Although the Ni/MgO catalyst has an improved CO pathway, the activation energy of its intermediates is still higher, making it less efficient overall.[109] Xu *et al.* also showcased the formate pathway on Ni. In the formate pathway, CO_2 initially adsorbs on the ZrO_2 surface to form carbonate species that are hydrogenated to formate (HCOO*). This intermediate is further hydrogenated with HCO*, H_2CO*, H_3CO*, and finally methane (CH_4). The ZrO_2 support, like MgO in the work by Jin Huang *et al.*, improves the stabilization of these intermediates by lowering the energy barriers of each step. In the CO pathway, CO_2 is initially converted to CO, which is then adsorbed on the Ni surface. Hydrogenation of CO occurs before methane formation through intermediates, such as COH*, CHO*, and CH*. Although ZrO_2 initially aids in the activation and reduction of CO_2 to CO, subsequent steps occur mostly on the Ni surface. The study finds that the formate pathway of the Ni/ZrO_2 catalyst has lower activation barriers than the CO pathway. The formation of formate on ZrO_2 is particularly favorable due to the energy barrier of approximately 0.65 eV. Subsequent hydrogenation steps on the Ni surface are also energetically feasible, maintaining a reasonable activation energy throughout the route. However, despite the initial facilitation of the ZrO_2 support, the CO pathway involves higher energy barriers for the intermediates COH*, CHO*, and CH*, making it less efficient. The activation energy of the rate-determining step of the formate pathway of the Ni/ZrO_2 catalyst is around 0.65 eV, which is lower than the activation energy of the unsupported Ni or Ni supported by other materials.[110]

A few control experiments were studied to assess the role of NiO at 300 °C under a mixture of CO_2 and H_2. As the stability studies were conducted at 300 °C, the same temperature was

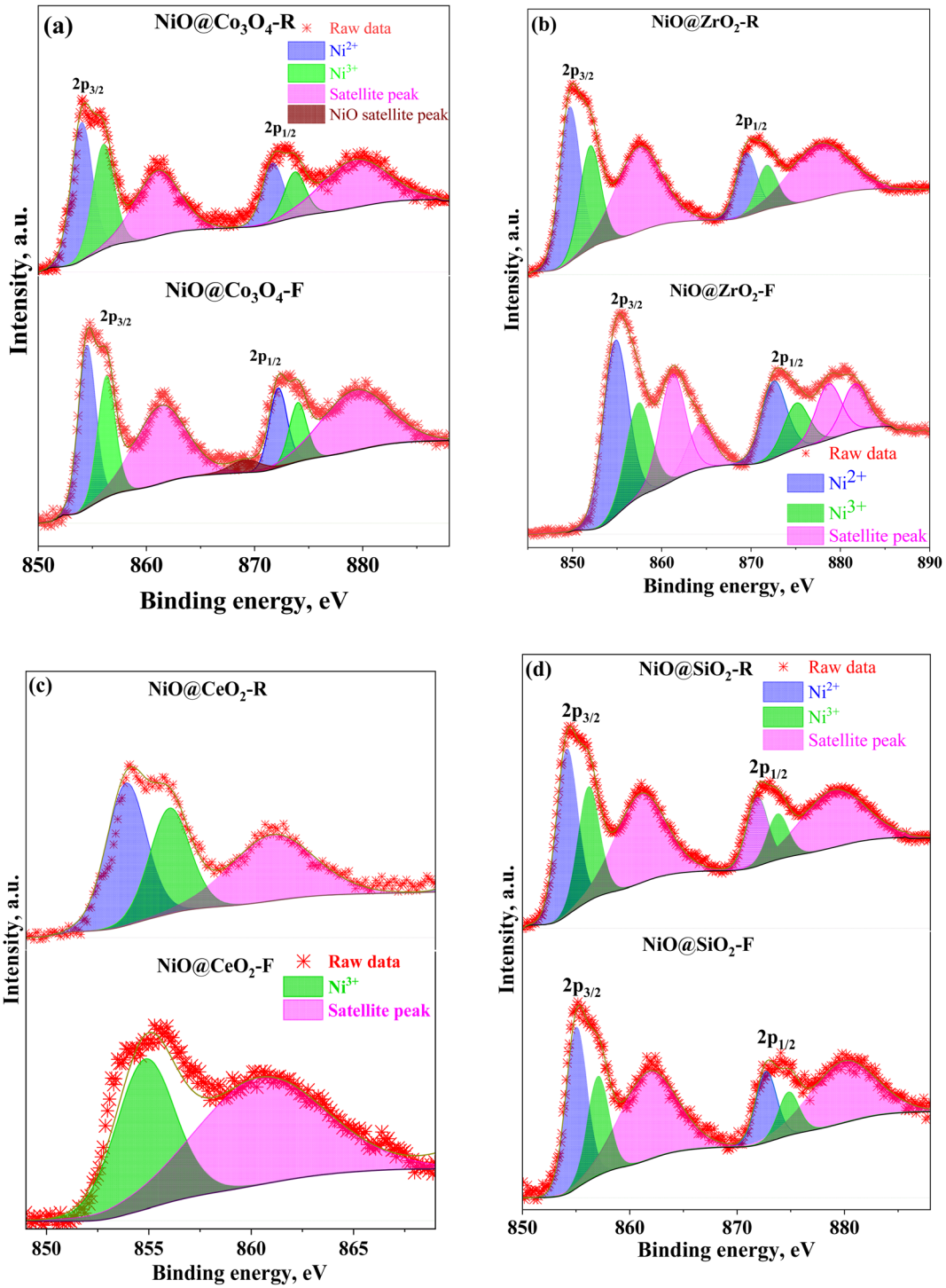

Fig. 8 Core level spectra of (a) Ni 2p NiO@Co_3O_4, (b) Ni 2p NiO@ZrO_2, (c) Ni 2p NiO@CeO_2, and (d) Ni 2p NiO@SiO_2 for both fresh (F) and reduced (R) materials.

chosen for the CO_2 and CO_2–H_2 mixture treatment in the control experiment on the reduced catalyst. The results are shown in Fig. S11.†

3.4.1. Control study 1. The catalyst was reduced at 400 °C in H_2, and CO_2 alone was passed at 300 °C for 1 h to oxidize the reduced Ni. Later, the material was cooled and degassed with Ar. Subsequently, the TPR step was conducted to remove lattice oxygen from the recreated NiO phase. All the control experiments were conducted *in situ* without ambient air exposure. After reoxidation of NiO@SiO_2 with CO_2, the reduction peaks were found at 165 °C and 260 °C. A similar experiment was performed on NiO, which was used as a core material in the synthesis. The reduction peak of the reoxidized NiO from the core material was observed at 207 °C. This proves the recreation

of NiO and its reduction. Interestingly, the lattice oxygen release was spread across wide temperatures after the reduction peak, indicating the possible NiO phase within the proximity of the operating temperatures of the reaction. The same trend was observed with NiO as well, and confirms the NiO formation due to CO_2.

3.4.2. Control study 2. The second control experiment was performed to evaluate the catalyst ability to recreate the NiO phase in the presence of the CO_2 and H_2 mixture. Although significant reduction peaks were not obtained, the reduction ability from the oxidized surface can be observed at temperatures up to 538 °C. This again confirms the formation of NiO due to CO_2 in the feed.

Considering the outcomes of the control experiments, simulations on NiO were performed to determine the role of the oxidized Ni. A geometric optimization was performed on the pristine NiO lattice to fully relax the system, as shown in Fig. S12.† DFT simulations were conducted to gain mechanistic insights for these reaction pathways after determining the stable locations of each species involved across the various reaction intermediate routes. Two different pathways were investigated for converting CO_2 into CH_4 on NiO. These can be categorized as pathway 1 and pathway 2, which involve the formation of HCOOH* and CO* as intermediate species.[108,111] The two pathways start with the adsorption of one molecule of CO_2 onto the O-Top site, followed by the simultaneous dissociation of one H_2 molecule and the adsorption of 2H atoms on the O-Top site, as shown in Fig. S13.† At this point, the surface has two adsorbed species on it, and the total energy of this system is taken as the reference point for the relative energy calculations (refer to Table S1†).

3.4.3. Pathway 1 (formate pathway). A complete reaction mechanism for pathway 1 is presented in Section S.2.1.† After successful adsorption of CO_2^* and H*, they react to form an intermediate species, HCOO*, in the bridge site on the surface (Fig. 9(a)). The energy difference for the formation of HCOO* is calculated to be 2.17 eV. The HCOO* further reacts with the remaining H* atom to form HCOOH* (Fig. 9(b)).

Another molecule of H_2 introduced to the system dissociates to form 2H atoms, which are then adsorbed onto the O-Top site

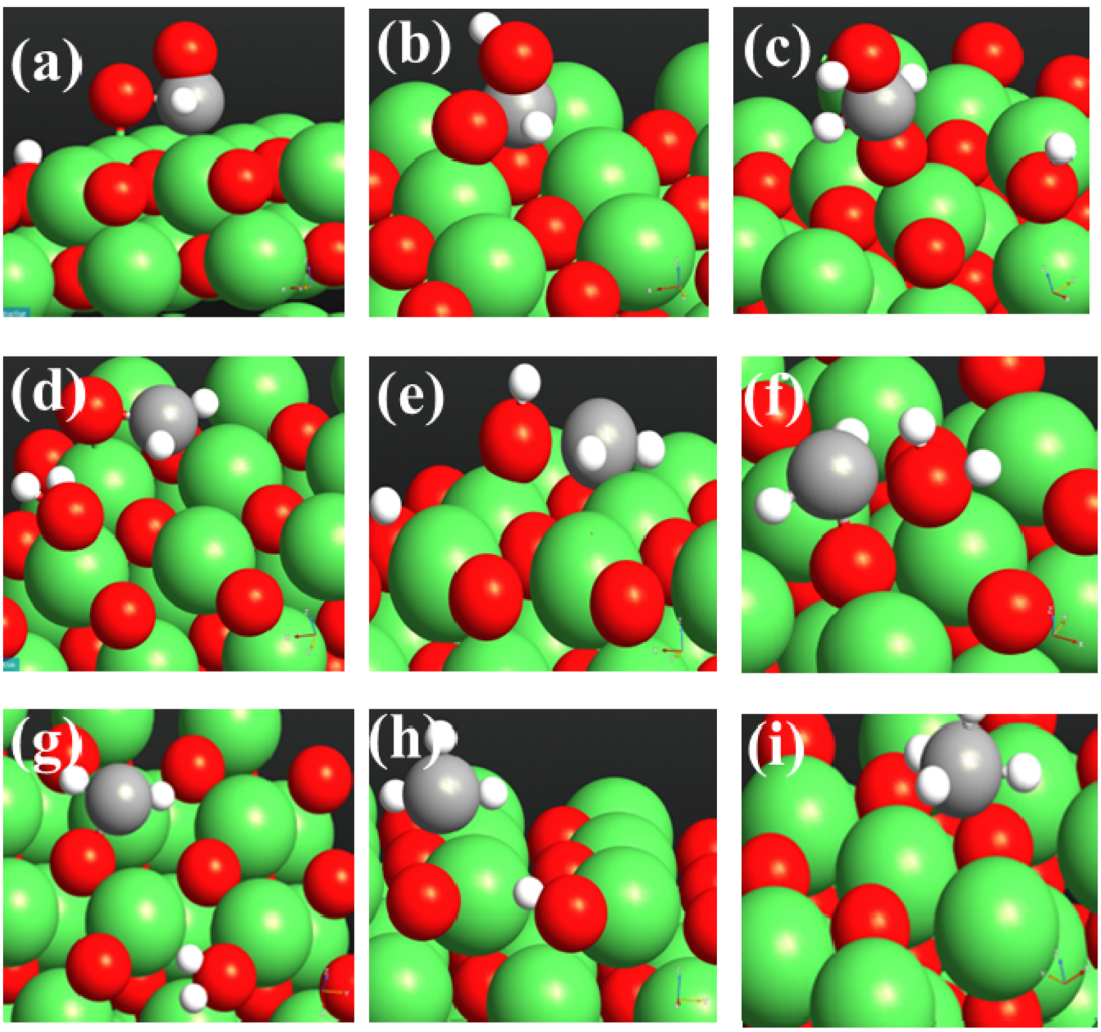

Fig. 9 Formation of (a) HCOO*, (b) HCOOH*, (c) H_2COOH*, (d) H_2CO* and H_2O*, (e) CH_2^* and OH*, (f) CH_2^* and H_2O*, (g) CH_2^* and 2H*, (h) CH_3^*, and (i) CH_4^* on the NiO (200) surface.

of the surface. H* reacts with HCOOH* to form H_2COOH* and H* with an energy difference of −0.482 eV. It should be noted that H_2COOH* is now adsorbed through its oxygen atom on the Ni-Top site (Fig. 9(c)). Interestingly, a dehydration reaction occurs, and H_2COOH* dissociates into H_2O* and H_2CO* (Fig. 9(d)). H_2O* and H_2CO* are adsorbed onto the Ni-Top and bridge sites. H_2O can desorb, and a new H_2 molecule is introduced to the system. The process repeats as H_2 is dissociated, and 2H atoms are adsorbed onto the O-Top sites. H_2CO* reacts with H* to form H_2COH*, and the energy released to achieve this is 1.28 eV. H_2COH* now dissociates into CH_2^* and OH*. CH_2^* is adsorbed onto the O-Top site and OH* onto the Ni-Top site (Fig. 9(e)). The energy required to achieve this is 0.156 eV. OH* reacts with the already existing H* to form H_2O*, which is later allowed to desorb (Fig. 9(f)). Following this, another H_2 molecule is introduced to the system, which subsequently gets dissociated into two H atoms that are adsorbed onto the O-Top sites of the surface (Fig. 9(g)). CH_2^* and H* now react to produce CH_3^* (Fig. 9(h)). The energy required to achieve this conversion is 1.11 eV. In the end, CH_3^* and the remaining H* atom react to produce CH_4^*, and the energy required to achieve this is 2.72 eV (Fig. 9(i)). After performing the DFT calculation for each intermediate step of pathway 1, an energetics diagram (Fig. S14†) was plotted to understand how the energies of each step vary with the initial step.

3.4.4. Pathway 2 (The CO pathway). The reaction mechanism of pathway 2 is presented in detail. Just like in pathway 1, pathway 2 transitions through the formation of carbon monoxide as an intermediate species.

After the initial adsorption of CO_2 onto the O-Top site, CO_2^* dissociates into CO* and O* (Fig. 10(a)). O* is adsorbed onto the Ni-Top site, while CO* resides at the same site. An H_2 molecule is introduced to the system, which dissociates into two H atoms, and these are then adsorbed onto the O-Top site (Fig. 10(b)). O* and the two H* atoms combine from H_2O*, which is later allowed to be desorbed from the surface (Fig. 10(c)). The only species remaining on the surface now is CO* (Fig. 10(d)), which dissociates into C* on the O-Top site and O* on the Ni-Top site. The energy required to achieve this was calculated to be 0.55 eV. This is followed by the adsorption of two H atoms on the O-Top site from the dissociation of an H_2 molecule. O* combines with one of the H* atoms to form OH*, which later combines with the remaining H* atom to form H_2O* (Fig. 10(e)). Yet again, H_2O* can desorb away from the catalyst's surface.

An H_2 molecule dissociates, and the two H atoms are adsorbed onto the O-Top site. The surface now consists of a C* atom and two H* atoms. The C* reacts with an H* atom to form CH* (Fig. 10(f)) with the release of 2.07 eV of energy. CH* reacts with the remaining H* atom to form CH_2^* (Fig. 10(g)). Finally, another molecule of H_2 dissociates into two H atoms that are adsorbed onto the O-Top site (Fig. 10(h)). CH_2^* reacts with the remaining H* atoms to form CH_3^* (Fig. 10(i)), and finally CH_4^* (Fig. 10(j)).

A similar approach to construct a reaction energetics plot was applied for pathway 2 to better understand the energetics of the reaction (Fig. S15†).

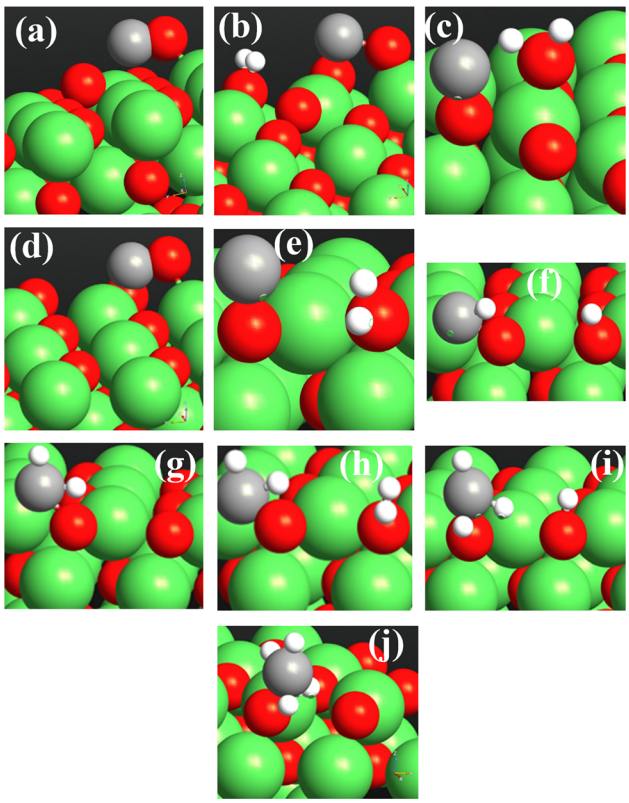

Fig. 10 Formation of (a) CO* and O*; (b) CO* and 2H*; (c) CO* and H_2O*; (d) CO*; (e) C* and H_2O*; (f) CH* and H*; (g) CH_2^*; (h) CH_2^* and $2H_2O$*; (i) CH_3^* and H*; (j) CH_4^* on the NiO (200) surface.

3.5. *In situ* FTIR study

Fig. 11 and 12 show the FTIR spectra of all core shell catalysts, where peaks ranging from 3725 cm^{-1} to 3591 cm^{-1} are identified and correlated as CO_2 overtones. This correlation demonstrates an understanding of the CO_2 molecular vibrational modes. In the composition of $CO_2:N_2$ (30 : 70 mL min^{-1}), the NiO@SiO_2 catalyst converts CO_2 into monodentate, and bidentate carbonates can be observed in Fig. 11(a). These intermediates are further reacted in the presence of H_2, and the formed distinct species can be seen in Fig. 12(a). The peak observed at 1560 cm^{-1} signifies the presence of the formate species. As the temperature was increased to 300 °C, the formate peak was diminished. Meanwhile, a subsequent increase occurred in the peak intensity at 1622 cm^{-1}, representing the bicarbonate species. This transition indicates the decomposition of formate, releasing hydrogen and generating bicarbonate. Further hydrogenation leads to the formation of the ν-CH stretching vibration, corresponding to the methane peak, which was observed at 3013 cm^{-1} and 1302 cm^{-1}. The peak intensity was found to increase as the temperature increases; this nature is implied in the formation of methane. The peak at 1872 cm^{-1} represents the bridged CO (ν-br-CO) on the Ni species.[112,113] The carbonate peaks observed at 1132.5 cm^{-1} and 1008 cm^{-1} correspond to the presence of both bidentate carbonate and bicarbonate species.[113] Fig. 11(b) depicts the FTIR spectra with CO_2 adsorption for the NiO@CeO_2

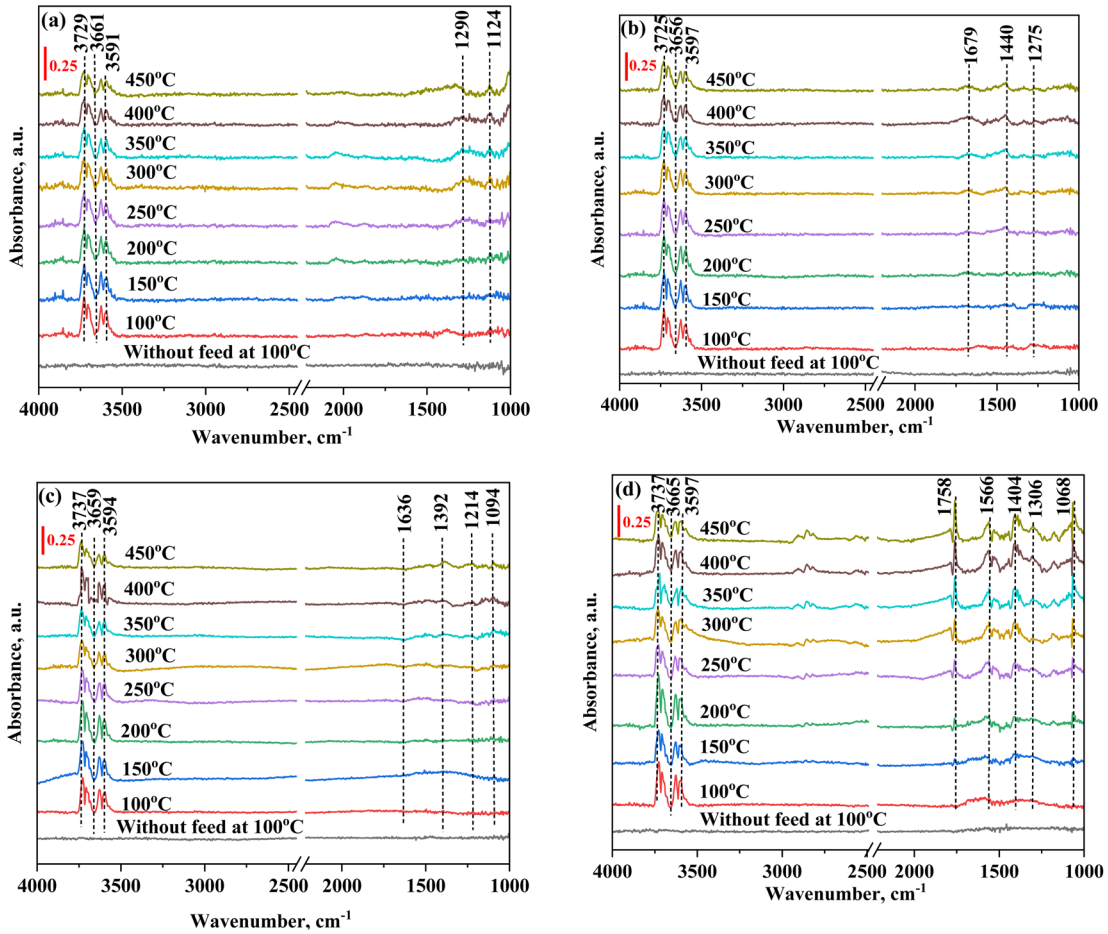

Fig. 11 *In situ* FTIR analysis of (a) NiO@SiO_2, (b) NiO@CeO_2, (c) NiO@Co_3O_4, and (d) NiO@ZrO_2 without H_2 flow (flow conditions: $CO_2 : N_2 = 30 : 70$ mL min^{-1}. The reduction conditions are maintained at 400 °C with an H_2 flowrate of 50 mL min^{-1} for 1 h).

catalyst without H_2 flow, with peaks at 1679 cm^{-1}, 1275 cm^{-1}, and 1440 cm^{-1} representing bidentate carbonate and bicarbonate species. In Fig. 12(b), when CO_2 and H_2 were reacted, the formation of formate at 1490 cm^{-1} was observed as an intermediate species. Subsequent hydrogenation resulted in the appearance of ν-CH stretching signals, identified as methane, at 3015 cm^{-1} and 1308 cm^{-1}. Peaks at 1655 cm^{-1} and 1490 cm^{-1} signify the asymmetric stretching vibration associated with CO adsorption (bidentate carbonate), along with the formate species, while the carbonate species were observed at 1183 cm^{-1}.[114,115] In Fig. 12(a) and (b), minor disturbances in the spectra were observed from 300 °C, which were attributed to moisture content, as water is a significant byproduct in the methanation reaction. In Fig. 11(c), the FTIR spectra of NiO@Co_3O_4 without H_2 flow reveals distinctive peaks at 1636 cm^{-1} and 1214 cm^{-1}, signifying the presence of bicarbonate species, while peaks at 1392 cm^{-1} and 1094 cm^{-1} indicate the presence of the carbonate species. Fig. 12(c) represents the FTIR spectra of NiO@Co_3O_4, which follows pathway 2 (CO pathway). CO_2 dissociated into CO* and O*, followed by hydrogenation, resulting in the emergence of ν-CH stretching vibration peaks at 3014 cm^{-1} and 1307 cm^{-1}, indicative of methane formation. Linear CO species were identified at 2182 cm^{-1} and 2214 cm^{-1}. Additionally, peaks at 1390 cm^{-1} and 1102 cm^{-1} signify the symmetric vibration characteristic of bicarbonate and carbonate species, respectively.[110,116] The FTIR spectra of NiO@ZrO_2, presented in Fig. 12(d), exhibited distinct features. Peaks at 3015 cm^{-1} and 2854 cm^{-1} were attributed to the ν-CH stretching characteristic of methane.[117,118] A notable observation was the emergence of a new peak at 1762 cm^{-1}, identified as the antisymmetric C=O stretching vibration. This was indicative of CO_2 adsorption in a COO^- state at the Ni site, denoted as the $CO_2^* - Ni$ species. This phenomenon was observed from 150 °C onwards, further facilitating the generation of CO on the NiO@ZrO_2 catalyst, as evidenced by peaks at 2187 cm^{-1} and 2106 cm^{-1}.[118] Additionally, a peak at 1566 cm^{-1} indicated the formation of the formate species. The spectrum also revealed peaks at 1566/1306 cm^{-1}, 1444 cm^{-1}, and 1068 cm^{-1}, corresponding to the asymmetric/symmetric stretching vibrations of carbonate, representing bidentate carbonate species, symmetric stretching vibration of monodentate carbonate, and bicarbonate species, respectively. Fig. 11(d) demonstrates a slight deviation in the carbonate species for the FTIR spectra of NiO@ZrO_2 without H_2 flow. Table S5† summarizes the infrared frequencies of the species

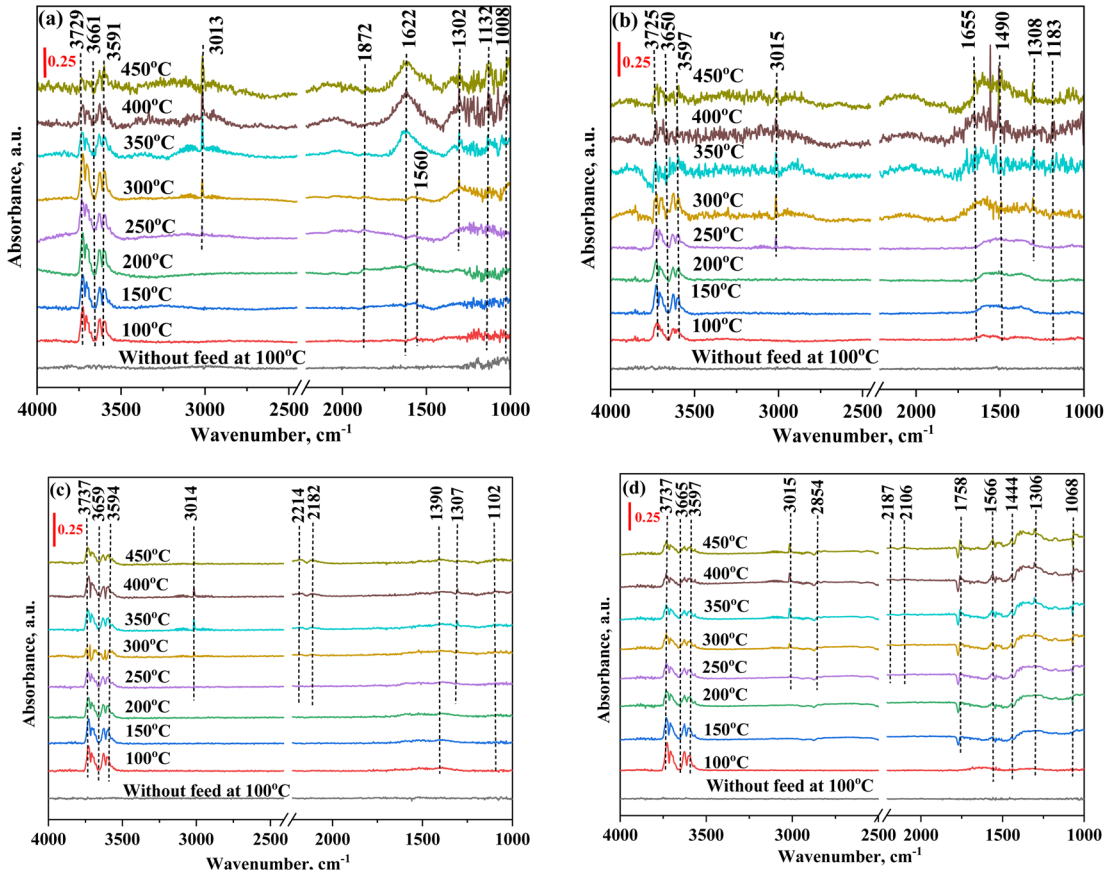

Fig. 12 *In situ* FTIR analysis of (a) NiO@SiO_2, (b) NiO@CeO_2, (c) NiO@Co_3O_4, and (d) NiO@ZrO_2 (flow conditions: $CO_2 : H_2 : N_2 = 10 : 40 : 50$ mL min^{-1}, and the reduction conditions are at 400 °C with an H_2 flowrate of 50 mL min^{-1} for 1 h).

observed for all catalysts from the *in situ* FTIR studies for CO_2 methanation.

In situ FTIR studies were conducted with and without H_2 reduction for understanding the pivotal role of oxygen vacancies. Detailed spectra of CO_2 adsorption over NiO@SiO_2 and NiO@CeO_2 are provided in Fig. S16,† with representative spectra at 350 °C and 400 °C. Bicarbonate (*CO_3H, 1008 and 1622 cm^{-1}) and bidentate carbonate (*CO_3, 1132 cm^{-1}) species, recognized as critical intermediates in methane formation, were observed. Samples not subjected to H_2 reduction exhibited lower signal intensities for the *CO_3H and *CO_3 species, indicating less effective intermediate formation. The formation of the *HCO_3 and *CO_3 intermediates across all samples demonstrates that the oxygen vacancies, created through thermal and reduction treatments, significantly enhance CO_2 adsorption.[24] Notably, a greater production of *CO, resulting from the conversion of *CO_3 and *HCO_3, was observed over reduced NiO@SiO_2, highlighting *CO as a key intermediate for methane production.[78,81] During the reduction process, CO_2 first adsorbs onto the surface and interacts with oxygen vacancies and *OH groups to form *CO_3 and *HCO_3. The *CO_3 species, adsorbed on oxygen vacancies, are then hydrogenated to form *CO, which subsequently migrates to the active Ni,[110] as confirmed by *in situ* FTIR experiments. These intermediates, particularly *HCO_3 on basic sites and *CO on Ni, undergo continuous hydrogenation, leading to methane formation on the catalyst surface. The literature predominantly discusses two mechanisms for CO_2 methanation: the dissociative pathway (*via* *CO formation) and the associative pathway (*via* the formation of bicarbonates, formates, and carboxyl species). Our findings suggest a novel oxygen-assisted mechanism that follows the dissociative pathway for CO_2 methanation. This study confirms that oxygen vacancies significantly influence the catalytic performance of Ni-based catalysts during CO_2 methanation.

From both DFT simulations and *in situ* FTIR findings, it was observed that NiO@S (where S = SiO_2, CeO_2, ZrO_2) follows both pathway 1 (formate pathway) and pathway 2, while NiO@Co_3O_4 only follows pathway 2 (CO pathway).

3.6. Characterization of spent catalyst

3.6.1. XRD analysis of spent catalyst. Fig. S17† shows the XRD pattern of the spent catalysts. When compared with the XRD analysis of the fresh catalysts, NiO has been transformed into metallic Ni (JCPDS file no.: 04-0850) with 2θ values of 45.0°, 52.4° and 76.8° that correspond to the (111), (200), and (220) lattice planes, respectively.[119] There was no change in the CeO_2 phase, as the 2θ values were 29.1°, 33.6°, 48.0°, 56.9°, corresponding to the (111), (220), (220), and (311) planes,

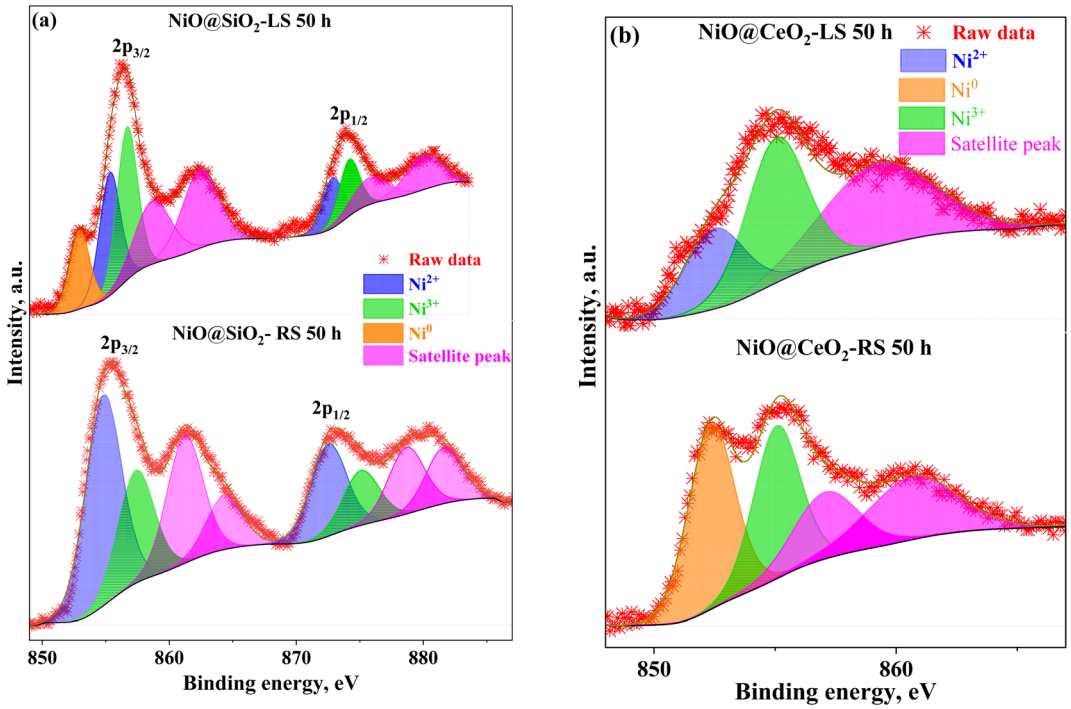

Fig. 13 XPS spectra of (a) Ni 2p NiO@SiO_2-50 h and (b) Ni 2p NiO@CeO_2-50 h for spent catalysts under lean feed (LS) and realistic feed (RS) conditions.

respectively. The XRD analysis (shown in Fig. S17†) for the spent catalysts (tested at high feed concentration) shows no alloy formation. This proves that the structural stability was retained even after the cyclic stability study.

3.6.2. XPS analysis of the spent catalyst. The XPS spectra of the spent catalyst after the stability study and cyclic study are depicted in Fig. 13. In Fig. 13(a), the XPS spectra of NiO@SiO_2 reveal a peak at 852.9 eV, indicative of metallic Ni, alongside peaks at $2p_{3/2}$ of Ni^{2+} at 855.3 eV, and Ni^{3+} at 856.7 eV. At $2p_{1/2}$, the Ni^{2+} peak was at 872.8 eV and the Ni^{3+} peak was at 874.3 eV, and the satellite peaks were at 858.8 eV, 862.3 eV, 876.1 eV and 880.3 eV for the lean stability (LS) condition. For the realistic stability (RS) condition, the Ni^{2+} and Ni^{3+} peaks were detected at 854.9 eV and 857.3 eV for the $2p_{3/2}$ orbital. For the $2p_{1/2}$ orbital, the peaks at 872.8 eV ad 875.2 eV correspond to Ni^{2+} and Ni^{3+} ions, respectively. In Fig. 13(b), the XPS spectra of the Ni peaks in NiO@CeO_2 exhibit peaks at 853.2 eV and 856.1 eV that represent the Ni^{2+} and Ni^{3+} ions, respectively. The satellite peak was observed at 861.4 eV for lean stability. Meanwhile, the peak at 855.1 eV represents the Ni^{3+} states, and satellite peaks at 857.1 and 860.9 eV were observed for the realistic stability condition. For NiO@SiO_2, after the stability study and cyclic study of 50 h, Si was observed in the 2p orbital at 103.2 eV, and is presented in Fig. S18(a).†[77,101] Fig. S18(b)† showcases the XPS spectra of NiO@CeO_2, where the peaks at 881.8, 885.6, and 898.1 eV correspond to Ce^{4+} of the $3d_{5/2}$ orbital. The peaks at 900.0, 904.0, and 917.0 eV correspond to Ce^{4+} of $3d_{3/2}$. The Ce^{3+} states were observed at 883.8 and 888.6 eV for $3d_{5/2}$. For $3d_{3/2}$, the peaks were observed at 902.1 and 907.2 eV for the lean stability condition. The binding energies corresponding to the realistic stability conditions were matched with the lean stability condition, indicating the robust stability of the catalysts. Furthermore, Fig. S19(a)† illustrates the O 1s spectra for NiO@SiO_2 with a peak at 531.4 eV attributed to lattice oxygen, another at 533.1 eV associated with Si–O–Si, and surface adsorbed oxygen for both lean and realistic conditions.[106] Conversely, Fig. S19(b)† displays slightly shifted O 1s spectra for NiO@CeO_2 at 530.8, 532.8, and 534.5 eV, corresponding to lattice oxygen, vacant oxygen, and satellite peaks, respectively. A decrement in the peak intensity for vacant oxygen was observed for realistic stability when compared to lean stability study. This indicates the catalyst deactivation under realistic feed conditions.

3.6.3. Insights into the structure–activity relationship. Analysis of the spent catalyst through SEM imaging revealed a noticeable reduction in the particle size compared to the fresh catalyst (shown in Fig. 14). This reduction can be attributed to particle sintering during the 50 hours stability study under high concentrated feed mixture. Additionally, agglomeration is evident, leading to the formation of larger particles. N_2 adsorption–desorption analysis corroborated these findings, indicating a slight decrease in the surface area (46 and 27 m^2 g^{-1} for spent NiO@SiO_2 and NiO@CeO_2, respectively) compared to the fresh catalyst (58 and 28 m^2 g^{-1} for fresh NiO@SiO_2 and NiO@CeO_2, respectively). This is likely due to the pore size reduction during the extended reaction period. Despite these minor changes, the catalysts continued to exhibit robust catalytic activity. The N_2 adsorption–desorption analysis of the spent catalyst is presented in Table S6.† The elemental mapping shown in Fig. S20† depicts the separation of Ni or NiO

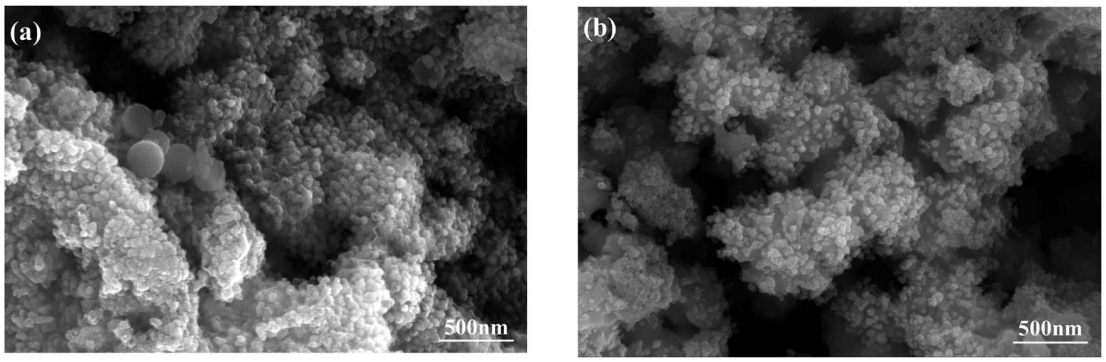

Fig. 14 SEM images of the (a) NiO@SiO_2 and (b) NiO@CeO_2 spent catalysts.

Table 4 CO_2 and H_2 adsorption and desorption of the catalysts at 25 °C

	CO_2 adsorption capacity at 298 K (mg of CO_2 per g)		H_2 adsorption capacity at 298 K (mg of H_2 per g)	
Catalyst	At 1 bar	At 50 bar	At 1 bar	At 50 bar
(a) NiO@SiO_2	30.33	301.96	0.06	0.74
(b) NiO@CeO_2	25.05	279.75	0.14	0.67
(c) NiO@ZrO_2	57.01	259.65	0.05	0.77
(d) NiO@Co_3O_4	90.40	227.66	0.15	1.01

from the shell metal oxide. XRD studies (Fig. S17†) for the spent catalyst showed the presence of CeO_2 in NiO@CeO_2. Considering the amorphous nature of silica, the SiO_2 was not observed in the diffraction patterns corresponding to NiO@SiO_2. In general, the phase separation leading to alloy formation deactivates the catalyst in the long run. The phase separation is clearly visible in the NiO@CeO_2 catalyst as separate Ni/NiO and CeO_2. However, NiO@SiO_2 retained its strong structural stability without any agglomeration or phase separation. Thus, catalysts with strong metal support interaction must be developed to retain the catalyst stability for long time-on-stream and large number of cycles.

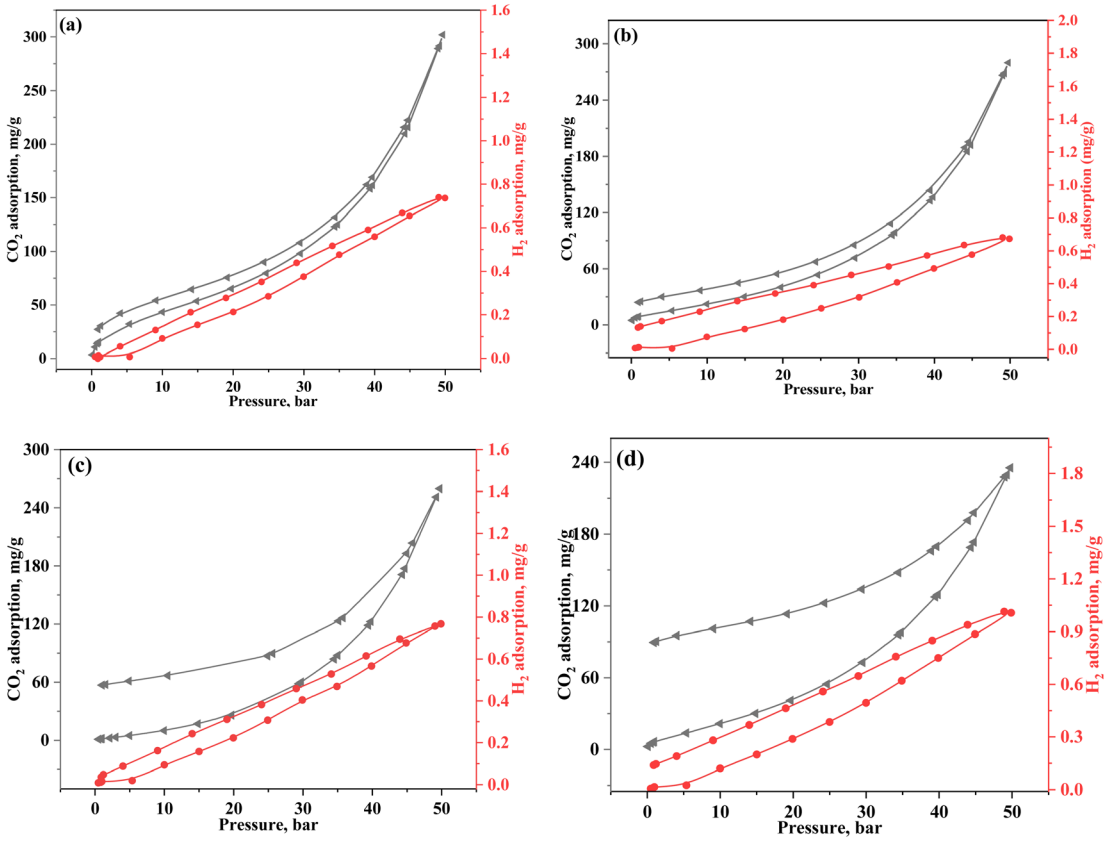

Fig. 15 CO_2 and H_2 adsorption and desorption at 298 K of (a) NiO@SiO_2, (b) NiO@CeO_2, (c) NiO@ZrO_2, and (d) NiO@Co_3O_4.

3.7. CO_2 and H_2 capture studies

Among the four catalysts analyzed through the BET surface area, NiO@SiO_2 exhibited the highest surface area. As corroborated by CO_2 TPD studies, NiO@SiO_2 has abundant weak basic sites, revealing its superior CO_2 capture performance at 301.96 mg of CO_2 per g at 25 °C and 50 bar.[120–122] From Table 4, it is clear that NiO@CeO_2 exhibits a significant CO_2 capture ability up to 279.75 mg of CO_2 per g. NiO@ZrO_2 demonstrated medium and strong basic sites at high temperatures, while NiO@Co_3O_4 exhibited medium basic sites, contributing to their respective levels of CO_2 adsorption of 259.65 and 227.66 mg of CO_2 per g. However, desorption does not occur as readily as adsorption of CO_2, as shown in Fig. 15. Desorption at 1 bar suggests that CO_2 is still retained within the catalyst, indicating its capacity to chemisorb or capture CO_2 at atmospheric pressure for CO_2 capture. Interestingly, this behaviour deviates from the adsorption trend during desorption at ambient temperature. *In situ* FTIR analysis further supports this phenomenon, revealing CO_2 adsorption at 1 bar. When monitoring the catalyst through *in situ* FTIR at varying temperatures under atmospheric pressure, intermediates can be observed in Fig. 12, such as carbonates, bidentate carbonate, and monodentate carbonate. NiO@Co_3O_4 has the highest CO_2 capture ability of 90.40 mg of CO_2 per g at 1 bar due to its greater pore volume of 0.23 $cm^3\ g^{-1}$. NiO@CeO_2 shows the lowest CO_2 capture of 25.05 mg of CO_2 per g at 1 bar. This provides insights into the mechanisms of CO_2 adsorption on the catalyst surface, and the ensuing reactions occurring solely in the presence of CO_2 at atmospheric pressure.

For H_2 adsorption, low values are observed due to the low adsorption affinity of H_2 gas.[123] NiO@Co_3O_4 shows high H_2 adsorption of 1.01 mg of H_2 per g at 50 bar and 25 °C, while NiO@CeO_2 shows the lowest H_2 ability of 0.67 mg of H_2 per g. While slight variations exist in the CeO_2 and ZrO_2 catalysts, substantial differences are not evident at both 50 and 1 bar. However, the trends for adsorption and desorption remain consistent. Notably, during desorption at 1 bar, these catalysts exhibit H_2 adsorption, indicating their chemisorption capability in retaining H_2 under atmospheric pressure. NiO@Co_3O_4 and NiO@CeO_2 exhibit nearly identical H_2 adsorption capacities, 0.15 and 0.14 mg of H_2 per g, respectively. The similar capture ability at low pressures may be due to their equivalent mean pore diameters.

4. Conclusions

The impact of several metal oxide shell materials on the Ni/NiO core was investigated. Both NiO@SiO_2 and NiO@CeO_2 were found to be the most effective catalysts for CO_2 methanation. After 300 °C, a diminishing trend in the conversion and selectivity was noticed in all active catalysts owing to competing side reactions. Stability studies revealed that both NiO@SiO_2 and NiO@CeO_2 are highly stable for 50 h under lean and rich CO_2 concentration in the feed. TPR studies showed that the oxygen storage capacity and redox nature of the catalysts play a vital role in activating CO_2 molecules. A moderate reducible nature of NiO@CeO_2 and NiO@SiO_2 (10.9 mmol g^{-1} and 10.0 mmol g^{-1}) was observed when compared to NiO@Co_3O_4 (17.6 mmol g^{-1}). Although the reducible nature is low, the large number of weak and medium basic sites of NiO@CeO_2 and NiO@SiO_2 contributed to enhancing the catalytic activity.

Two mechanisms through DFT studies were observed to be prominent in dissociating CO_2 to form carbonyl groups. Ni plays an active role in forming transition states at lower free energies than NiO. However, as Ni easily gets reoxidized (as proven from the control experiments), the role of lattice oxygen in reoxidized NiO was also assessed in the reaction mechanism. Furthermore, the intermediates (atomic oxygen, atomic hydrogen, CO, CH_4, H_2, O_2 and H_2O) considered in the reaction pathways of DFT are identified using CO_2-TPD-MS by replicating the similar conditions of the catalyst pre-treatment. The CO_2 methanation mechanism on these catalysts is elucidated through a combination of *in situ* FTIR spectra, CO_2-TPD-MS and DFT studies, offering valuable insights into the reaction pathways. The formate pathway from DFT studies correlated with the mechanism observed in the FTIR spectra of the following catalysts NiO@S (where, S = SiO_2, CeO_2, ZrO_2), while the NiO@Co_3O_4 catalyst showed the CO pathway alone. CO_2 and H_2 adsorption studies were conducted in the pressure range of 1–50 bar. At 50 bar, NiO@SiO_2 exhibits the highest CO_2 adsorption capacity of 301.96 mg of CO_2 per g, whereas at 1 bar, NiO@Co_3O_4 captures 90.40 mg of CO_2 per g. Both high OSC materials (NiO@CeO_2 and NiO@Co_3O_4) showed higher H_2 uptake than others at 1 bar. However, NiO@Co_3O_4 continued to outperform other materials at 50 bar. Although the H_2 and CO_2 capture ability of NiO@SiO_2 and NiO@CeO_2 is moderate, the large number of low and medium strength basic sites contributed to its superior catalytic activity. Among all catalysts, NiO@SiO_2 has offered the best catalytic activity with the lowest apparent activation energy of 82.0 ± 2 kJ mol^{-1}.

Data availability

The data supporting this article have been included as part of the ESI.†

Conflicts of interest

The authors state that they have no known conflicting financial interests or personal ties that may have seemed to influence the work presented in this study.

Acknowledgements

S. A. S. thanks the Science & Engineering Research Board (SERB), Department of Science and Technology (Grant No. CRG/2021/000333) for their financial support. Y. V. and L. Y. thank the BITS-Pilani Hyderabad campus for providing institute fellowships. The authors are grateful for the characterization facilities offered by the Central Analytical Laboratory, BITS-Pilani Hyderabad Campus. S. A. S. thanks DST-PURSE (Grant No. SR/PURSE/2020/20(G)) and DST-FIST (Grant No. SR/FST/ET-

I/2021/918(C)) for funding the *in situ* FTIR and chemisorption facilities, respectively.

References

1 D. Gielen, F. Boshell, D. Saygin, M. D. Bazilian, N. Wagner and R. Gorini, *Energy Strategy Rev.*, 2019, **24**, 38–50.
2 F. Perera, *Int. J. Environ. Res. Public Health*, 2018, **15**(1), 16.
3 W. F. Lamb, T. Wiedmann, J. Pongratz, R. Andrew, M. Crippa, J. G. J. Olivier, D. Wiedenhofer, G. Mattiolo, A. A. Khourdajie, J. House, S. Pachauri, M. Figueroa, Y. Saheb, R. Slade, K. Hubacek, L. Sun, S. K. Ribeiro, S. Khennas, S. D. L. R. D. Can, L. Chapungu, S. J. Davis, I. Bashmakov, H. Dai, S. Dhakal, X. Tan, Y. Geng, B. Gu and J. Minx, *Environ. Res. Lett.*, 2021, **16**(7), 73005.
4 J. Yuan, R. Fu, Z. Wang, X. Zheng, Y. Wang, H. Yan, Y. Liu, Y. Qu, G. Zhang, B. Sun, L. Wang, W. Xu, X. Feng, D. Chen and C. Yang, *ACS Catal.*, 2024, **14**, 11045–11050.
5 Y. Yang, Y. Li, Y. Lu, Z. Chen and R. Luo, *ACS Catal.*, 2024, **14**, 10344–10354.
6 X. Zhu, T. Ge, F. Yang, M. Lyu, C. Chen and D. O. Hare, *J. Mater. Chem. A*, 2020, **8**, 16421–16428.
7 S. Wang, C. An and Q. H. Zhang, *J. Mater. Chem. A*, 2013, **1**, 3540–3550.
8 R. Aniruddha, V. M. Shama, I. Sreedhar and C. M. Patel, *J. Cleaner Prod.*, 2022, **350**, 131478.
9 R. Aniruddha, I. Sreedhar and B. M. Reddy, *J. CO_2 Util.*, 2022, **64**, 102182.
10 R. Aniruddha, I. Sreedhar and R. Parameshwaran, *Mater. Today: Proc.*, 2023, **72**, 74–80.
11 B. Wang, M. Mikhail, S. Cavadias, M. Tatoulian, P. D. Costa and S. Ognier, *J. CO_2 Util.*, 2021, **46**, 101471.
12 K. Sawahara, K. Yatagai, T. Boll and A. P. R. Gemma, *Int. J. Hydrogen Energy*, 2022, **47**, 19051–19061.
13 F. Zhang and P. Sun, *Int. J. Chem. Kinet.*, 2021, **53**, 946–953.
14 W. Gac, W. Zawadzki, G. Słowik, M. Kusmierz and S. Dzwigaj, *Appl. Surf. Sci.*, 2021, **564**, 150421.
15 W. Li, K. Wang, G. Zhan, J. Huang and Q. Li, *ACS Sustain. Chem. Eng.*, 2020, **8**, 14058–14070.
16 K. Stangeland, D. Kalai, H. Li and Z. Yu, *Energy Procedia*, 2017, **105**, 2022–2027.
17 A. Chel and G. Kaushik, *Alexandria Eng. J.*, 2018, **57**, 655–669.
18 P. Summa, K. Swirk, D. Wierzbicki, M. Motak, I. Alxneit, M. Ronning and P. D. Costa, *Molecules*, 2021, **26**, 6506.
19 M. Bailera, P. Lisbona, L. M. Romeo and S. Espatolero, *Renewable Sustainable Energy Rev.*, 2017, **69**, 292–312.
20 J. Wu, Y. Huang, W. Ye and Y. Li, *Adv. Sci.*, 2017, **4**, 1700194.
21 F. Geppert, D. Liu, M. V. E. Jansen, E. Weidner, C. Buisman and A. Heijne, *Trends Biotechnol.*, 2016, **34**, 879–894.
22 N. Aryal, T. Kvist, F. Ammam, D. Pant and L. D. M. Ottosen, *Bioresour. Technol.*, 2018, **264**, 359–369.
23 M. Thema, F. Bauer and M. Sterner, *Renewable Sustainable Energy Rev.*, 2019, **112**, 775–787.
24 J. Ren, F. Zeng, C. Mebrahtu and R. Palkovits, *J. Catal.*, 2022, **405**, 385–390.
25 A. I. Tsiotsias, N. D. Charisiou, E. Harkou, S. Hafeez, G. Manos, A. Constantiou, A. G. S. Hussien, A. A. Dabbawala, V. Sebastian, S. J. Hinder, M. A. Baker, K. Polychronopoulou and M. A. Goula, *Appl. Catal., B*, 2022, **318**, 121836.
26 K. P. Kuhl, T. Hatsukade, E. R. Cave, D. N. Abram, J. Kibsgaard and T. F. Jaramillo, *J. Am. Chem. Soc.*, 2014, **136**, 14107–14113.
27 H. Yoshida, T. Nakajima, Y. Yazawa and T. Hattori, *Appl. Catal., B*, 2007, **71**, 70–79.
28 M. Tahir, *J. CO_2 Util.*, 2020, **37**, 134–146.
29 C. Shao, W. Li, Q. Lin, Q. Huang and D. Pi, *Energy Technol.*, 2017, **5**, 604–610.
30 A. I. Tsiotsias, N. D. Charisiou, I. V. Yentekakis and M. A. Goula, *Catalysts*, 2020, **10**, 812.
31 G. C. Mao, X. T. Kan, M. X. Xiao, W. L. Liu, B. X. Dong and Y. L. Teng, *Ind. Eng. Chem. Res.*, 2022, **61**, 10124–10132.
32 C. Liang, X. Hu, T. Wei, P. Jia, Z. Zhang, D. Dong, S. Zhang, Q. Liu and G. Hu, *Int. J. Hydrogen Energy*, 2019, **44**, 8197–8213.
33 J. B. Branco, P. E. Brito and A. C. Ferreira, *J. Chem. Eng.*, 2020, **380**, 122465.
34 W. Ahmad, M. N. Younis, R. Shawabkeh and S. Ahmed, *Catal. Commun.*, 2017, **100**, 121–126.
35 A. I. Tsiotsias, N. D. Charisiou, I. V. Yentekakis and M. A. Goula, A review, *Nanomaterials*, 2021, **11**, 1–34.
36 L. Zeng, Y. Wang, Z. Li, Y. Song, J. Zhang, J. Wang, X. He, C. Wang and W. Lin, *ACS Appl. Mater. Interfaces*, 2020, **12**, 17436–17442.
37 W. K. Fan and M. Tahir, A Review, *Ind. Eng. Chem. Res.*, 2021, **60**, 13149–13179.
38 C. Zhou, Y. Nan, F. Zha, H. Tian, X. Tang and Y. Chang, *J. Fuel Chem. Technol.*, 2021, **49**, 1444–1457.
39 M. C. Bacariza, I. Graca, J. M. Lopes and C. Henriques, *ChemCatChem*, 2019, **11**, 2388–2400.
40 R. G. Chaudhuri and S. Paria, *Chem. Rev.*, 2012, **112**, 2373–2433.
41 M. C. Daniel and D. Astruc, *Chem. Rev.*, 2004, **104**, 293–346.
42 F. Caruso, *Adv. Mater.*, 2001, **13**, 11–22.
43 T. Gholami, M. S. Niasari, M. Bazarganipour and E. Noori, *Superlattices Microstruct.*, 2013, **61**, 33–41.
44 V. Chiozzi and F. Rossi, *Nanoscale Adv.*, 2020, **2**, 5090–5105.
45 T. A. Le, J. Kim, J. K. Kang and E. D. Park, *Catal. Today*, 2020, **356**, 622–630.
46 J. Ilsemann, A. S. Eifert, J. Friedland, L. Kiewidt, J. Thoming, M. Baumer and R. Guttel, *ChemCatChem*, 2019, **11**, 4884–4893.
47 Y. T. Li, L. Zhou, W. G. Cui, Z. F. Li, W. Li and T. L. Hu, *J. CO_2 Util.*, 2022, **62**, 102093.
48 J. Cored, A. G. Ortiz, S. Iborra, M. J. Climent, L. Liu, C. H. Chuang, T. S. Chan, C. Escudero, P. Concepcion and C. Avelino, *J. Am. Chem. Soc.*, 2019, **141**, 19304–19311.
49 J. P. Perdew, K. Burke and M. Ernzerh, *Phys. Rev. Lett.*, 1996, **77**, 3865–3868.
50 W. Kohn and L. J. Sham, *Phys. Rev.*, 1965, **140**, A1133–A1138.

51 P. E. Blochl, *Phys. Rev. B:Condens. Matter Mater. Phys.*, 1994, **50**, 17953–17979.
52 J. D. Head and M. C. A. Zerner, *Chem. Phys. Lett.*, 1985, **122**, 264–270.
53 H. J. Monkhorst and J. D. Pack, *Phys. Rev. B*, 1976, **13**, 5188–5192.
54 J. J. Varghese and S. H. Mushrif, *J. Phys. Chem. C*, 2017, **121**, 17969–17981.
55 P. G. Lustemberg, Z. Mao, A. Salcedo, B. Irigoyen, M. V. G. Pirovano and C. T. Campbell, *ACS Catal.*, 2021, **11**, 10604–10613.
56 D. Parimi, V. Sundararajan, O. Sadak, S. Gunasekaran, S. S. Mohideen and A. Sundaramurthy, *ACS Omega*, 2019, **4**, 104–113.
57 L. M. N. C. Alves, M. P. Almedia, M. Ayala, C. D. Watson, G. Jacobs, R. C. R. Neto, F. B. Noronha and L. V. Mattos, *Chem. Eng. Sci.*, 2021, **239**, 116604.
58 S. A. Singh, S. Mukherjee and G. Madras, *Mol. Catal.*, 2019, **466**, 167–180.
59 L. K. Wu, W. Y. Wu, H. Z. Cao, G. Y. Hou, Y. P. Tang and G. Q. Zheng, *J. Mater. Chem. A*, 2017, **5**, 10669–10677.
60 P. Bindu and S. Thomas, *J. Theor. Appl. Phys.*, 2014, **8**, 123–134.
61 C. Hu, M. Yoshida, H. C. Chen, S. Tsunekawa, Y. F. Lin and J. H. Huang, *Chem. Eng. Sci.*, 2021, **235**, 116451.
62 V. Nandal, R. Sarvesha, S. S. Singh, E. W. Huang, Y. J. Chang, A. C. Yeh, S. Neelakantan and J. Jain, *J. Alloys Compd.*, 2021, **855**, 157521.
63 S. Tuti, I. Luisetto, U. P. Laverdura and E. Marconi, *Reactions*, 2022, **3**, 333–351.
64 K. Shanmuganandam, S. Thanikaikarasan, T. Ahamad, S. Ali and V. P. Sundramurthy, *Nanomaterials*, 2022, **2022**, 1–9.
65 J. Grams, R. Ryczkowski, K. Chalupka, I. Sobczak, I. Rzeznicka and K. Przybysz, *Materials*, 2019, **12**, 3792.
66 Y. Han, B. Wen and M. Zhu, *Catalysts*, 2017, **7**, 21.
67 R. P. Rocha, M. F. R. Pereira and J. L. Figueiredo, *Catal. Today*, 2023, **418**, 114136.
68 C. Dong, R. Mu, R. Li, J. Wang, T. Song, Z. Qu, Q. Fu and X. Bao, *J. Am. Chem. Soc.*, 2023, **145**(31), 17056–17065.
69 S. A. Singh, Y. Varun, P. Goyal, I. Sreedhar and G. Madras, *Catalysts*, 2023, **13**, 838.
70 Y. Varun, I. Sreedhar and S. A. Singh, *J. Environ. Chem. Eng.*, 2022, **10**, 108384.
71 Y. Varun, I. Sreedhar and S. A. Singh, *Mater. Today Proc.*, 2022, **72**, 417–424.
72 I. Sreedhar, Y. Varun, S. A. Singh, A. Venugopal and B. M. Reddy, *Catal. Sci. Technol.*, 2019, **9**, 4478–4504.
73 X. Wang, L. Zhu, Y. Liu and S. Wang, *Sci. Total Environ.*, 2018, **625**, 686–695.
74 X. Wang, L. Zhu, Y. Zhuo, Y. Zhu and S. Wang, *ACS Sustain. Chem. Eng.*, 2019, **7**, 14647–14660.
75 B. Wang, X. Zhu, S. Li, M. Chen, H. Lu and Y. Yang, *Nanomaterials*, 2018, **8**, 701.
76 A. J. Graham, P. V. Nguyen, H. Park, J. Nunn, V. Kandyba, M. Cattelan, A. Giampietri, A. Barinov, X. Xu, D. H. Cobden and N. R. Wilson, *2D Mater.*, 2024, **11**, 045021.
77 S. A. Singh, K. Vishwanath and G. Madras, *ACS Appl. Mater. Interfaces*, 2017, **9**, 19380–19388.
78 L. Ma, R. Ye, Y. Huang, T. R. Reina, X. Wang, C. Li, X. L. Zhang, M. Fan, R. Zhang and J. Liu, *Chem. Eng. J.*, 2022, **446**, 137031.
79 M. B. Peiro, J. Guilera and T. Andreu, *Chem. Eng. J.*, 2022, **433**, 133638.
80 Y. Du, C. Qin, Y. Xu, D. Xu, J. Bai, G. Ma and M. Ding, *Chem. Eng. J.*, 2021, **418**, 129402.
81 J. Ren, C. Mebrahtu, L. Koppen, F. Martinovic, J. P. Hofmann, E. J. M. Hensen and R. Palkovits, *Chem. Eng. J.*, 2021, **426**, 131760.
82 X. Chen, S. Ullah, R. Ye, C. Jin, H. Hu, F. Hu, Y. Peng, Z. H. Lu, G. Feng, L. Zhou and R. Zhang, *Energy Fuels*, 2023, **37**, 3865–3874.
83 A. Quindimil, U. D. L. Torre, B. P. Ayo, A. D. Quinonero, E. B. Garcia, D. L. Castello, J. A. G. Marcos, A. B. Lopez and J. R. G. Velasco, *Catal. Today*, 2020, **356**, 419–432.
84 J. Wu, Z. Jin, B. Wang, Y. Han, Y. Xu, Z. Liang and Z. Wang, *Ind. Eng. Chem. Res.*, 2019, **58**, 20536–20542.
85 X. Jia, X. Zhang, N. Rui, X. Hu and C. J. Liu, *Appl. Catal., B*, 2019, **244**, 159–169.
86 X. Lin, S. Wang, W. Tu, Z. Hu, Z. Ding, Y. Hou, R. Xu and W. Dai, *Catal. Sci. Technol.*, 2019, **9**, 731–738.
87 G. D. Piano, J. J. A. Gamboa, A. M. Condo and F. C. Gennari, *Int. J. Hydrogen Energy*, 2024, **56**, 1007–1019.
88 H. Fu, S. Sun and H. Lian, *J. CO_2 Util.*, 2023, **69**, 102415.
89 P. B. Weisz and C. D. Prater, *Adv. Catal.*, 1954, **6**, 143–196.
90 N. Rui, X. Zhang, F. Zhang, Z. Liu, X. Cao, Z. Xie, R. Zou, S. D. Senanayake, Y. Yang, J. A. Rodriguez and C. J. Liu, *Appl. Catal., B*, 2021, **282**, 119581.
91 Z. Fan, K. Sun, N. Rui, B. Zhao and C. Liu, *J. Energy Chem.*, 2015, **24**, 655–659.
92 Y. Xu, Y. Chen, J. Zhou, M. Song, X. Zhang and Y. Yin, *Int. J. Hydrogen Energy*, 2017, **42**, 13085–13091.
93 S. A. Singh, G. Madras and I. Sreedhar, *Top. Catal.*, 2021, **64**, 243–255.
94 M. A. A. Aziz, A. A. Jalil, S. Triwahyono, R. R. Mukti, Y. H. T. Yap and M. R. Sazegar, *Appl. Catal., B*, 2014, **147**, 359–368.
95 X. Geng, D. Lahem, C. Zhang, C. J. Li, M. G. Olivier and M. Debliquy, *Ceram. Int.*, 2019, **45**, 4253–4261.
96 V. M. Shinde and G. Madras, *AIChE J.*, 2014, **60**, 1027–1035.
97 U. Kwon, B. G. Kin, D. C. Nguyen, J. H. Park, N. Y. Ha, S. J. Kim, S. H. Ko, S. Lee, D. Lee and H. J. Park, *Sci. Rep.*, 2016, **6**, 30759.
98 K. Michalska, P. Kowalik, W. Prochniak and T. Borowiecki, *Catal. Lett.*, 2018, **148**, 972–978.
99 G. Zhi, X. Guo, Y. Wang, G. Jin and X. Guo, *Catal. Commun.*, 2011, **16**, 56–59.
100 S. A. Singh, B. Vemparala and G. Madras, *J. Environ. Chem. Eng.*, 2015, **3**, 2684–2696.
101 S. A. Singh and G. Madras, *Appl. Catal., A*, 2015, **504**, 463–475.
102 L. Xiao, J. A. Spies, C. J. Sheehan, Z. Zeng, Y. Gao, T. Gao, A. Ehrlacher, M. W. Zuerch, G. W. Brudvig and T. E. Mallouk, *J. Am. Chem. Soc.*, 2024, **146**, 18117–18127.

103 S. H. Pamu, K. B. S. Vashist, P. S. Ganesh, P. D. Costa and S. A. Singh, *Catal. Today*, 2024, **441**, 114841.
104 X. Wang, W. Yan, H. Li and Z. Wang, Nitrogen-Doped Ni/TiO_2 Catalyst with Enhanced Activity and Improved Selectivity for CO_2 Methanation, *Energy Fuels*, 2022, **36**, 11647–11653.
105 K. I. Maslakov, Y. A. Teterin, A. J. Popel, A. Y. Teterin, K. E. Ivanov, S. N. Kalmykov, V. G. Petrov, P. K. Petrov and I. Farnan, *Appl. Surf. Sci.*, 2018, **448**, 154–162.
106 X. Chen, Q. Wu, D. H. Kuo, A. B. Abdeta, H. Zhang, P. Li, T. Huang, O. A. Zelekew and J. Lin, *J. Mater. Chem. A*, 2023, **11**, 4126–4141.
107 I. A. Ivanin, O. V. Udalova, I. Y. Kaplin and M. I. Shilina, *Appl. Surf. Sci.*, 2024, **655**, 159577.
108 J. Ren, H. Guo, J. Yang, Z. Qin, J. Lin and Z. Li, *Appl. Surf. Sci.*, 2015, **351**, 504–516.
109 J. Huang, X. Li, X. Wang, X. Fang, H. Wang and X. Xu, *J. CO_2 Util.*, 2019, **33**, 55–63.
110 X. Xu, Y. Tong, J. Huang, J. Zhu, X. Fang, J. Xu and X. Wang, *Fuel*, 2021, **283**, 118867.
111 Y. Yang, J. Liu, F. Liu and D. Wu, *Fuel*, 2020, **276**, 118093.
112 R. P. Ye, W. Gong, Z. Sun, Q. Sheng, X. Shi, T. Wang, Y. Yao, J. J. Razink, L. Lin, Z. Zhou, H. Adidharma, J. Tang, M. Fan and Y. G. Yao, *Energy*, 2019, **188**, 116059.
113 Y. Zhao, V. Girelli, O. Ersen and D. P. Debecker, *J. Catal.*, 2023, **426**, 283–293.
114 L. P. L. Goncalves, J. Mielby, O. S. G. P. Soares, J. P. S. Sousa, D. Y. Petrovykh, O. I. Lebedev, M. F. R. Pereira, S. Kagnaes and Y. V. Kolenko, *Appl. Catal., B*, 2022, **312**, 121376.
115 Z. Bian, Y. M. Chan, Y. Yu and S. Kawi, *Catal. Today*, 2020, **347**, 31–38.
116 M. Wang, G. Zhang, J. Zhu, W. Li, J. Wang, K. Bian, Y. Liu, F. Ding, C. Song and X. Guo, *Chem. Eng. J.*, 2022, **446**, 137217.
117 A. Efremova, T. Rajkumar, A. Szamosvolgyi, A. Sapi, K. Baan, I. Szenti, J. G. Perez, G. Varga, J. Kiss, G. Halasi, A. Kukuovace and Z. Konya, *J. Phys. Chem. C*, 2021, **125**, 7130–7141.
118 L. M. N. C. Alves, M. P. Almeida, M. Ayala, C. D. Watson, G. Jacobs, R. C. R. Neto, F. B. Noronha and L. V. Mattos, *Chem. Eng. Sci.*, 2021, **239**, 116604.
119 J. Li, P. Li, J. Li, Z. Tian and F. Yu, *Catalysts*, 2019, **9**, 506–518.
120 B. Ashourirad, P. Arab, T. Islamoglu, K. A. Cychosz, M. Thommes and H. M. E. Kaderi, *J. Mater. Chem. A*, 2016, **4**, 14693–14702.
121 T. R. Menezes, K. M. C. Santos, T. S. L. Silva, K. S. Santos, A. L. Ramos, G. R. Borges, E. Franceschi, C. Dariva, J. F. D. Conto, S. M. Egues and C. C. Santana, *Gas Sci. Eng.*, 2023, **119**, 205136.
122 A. Chowdhury, S. Bhattacharjee, R. Chatterjee and A. Bhaumik, *J. CO_2 Util.*, 2022, **65**, 102236.
123 T. G. Kim, D. W. Lee, C. H. Lee, Y. S. Hong and J. K. Suh, *Korean J. Chem. Eng.*, 2023, **40**, 2463–2471.